

# CO observations and investigation of triggered star formation towards N10 infrared bubble and surroundings

D.R.G. Gama, J.R.D. Lepine and E. Mendoza

*Departamento de Astronomia do IAG/USP, Sao Paulo - Brazil*

Y. Wu

*University of Peking, Beijing - China*

ywu@pku.edu.cn

and

J. Yuan

*National Astronomical Observatories of China (NAOC)*

## ABSTRACT

We studied the environment of the dust bubble N10 in molecular emission. Infrared bubbles, first detected by the GLIMPSE survey at  $8.0\ \mu\text{m}$ , are ideal regions to investigate the effect of the expansion of the HII region on its surroundings eventual triggered star formation at its borders. In this work, we present a multi-wavelength study of N10. This bubble is especially interesting as infrared studies of the young stellar content suggest a scenario of ongoing star formation, possibly triggered, on the edge of the HII region. We carried out observations of  $^{12}\text{CO}(1-0)$  and  $^{13}\text{CO}(1-0)$  emission at PMO 13.7-m towards N10. We also analyzed the IR and sub-mm emission on this region and compare those different tracers to obtain a detailed view of the interaction between the expanding HII region and the molecular gas. We also estimated the parameters of the denser cold dust condensation and of the ionized gas inside the shell. Bright CO emission was detected and two molecular clumps were identified, from which we have derived physical parameters. We also estimate the parameters for the densest cold dust condensation and for the ionized gas inside the shell. The comparison between the dynamical age of this region and the fragmentation time scale favors the “Radiation-Driven Implosion” mechanism of star formation. N10 reveals to be specially interesting case with gas structures in a narrow frontier between HII region and surrounding molecular material, and with a range of ages of YSOs situated in region indicating triggered star formation.

*Subject headings:* ISM: bubbles — ISM: HII regions — ISM: molecules — stars: formation

## 1. Introduction

In the last decade the studies about massive star forming regions have gained considerable attention. Questions as whether the interaction of massive stars with their surrounding molecular clouds triggers the star formation have been amply discussed. The discovery of the “infrared bubbles”, a new type of object first

cataloged through the GLIMPSE<sup>1</sup> (Benjamin et al. 2003; Churchwell et al. 2009) at  $8.0\ \mu\text{m}$ , offers a new powerful tool to investigate the star formation process. Those objects present a bright border at  $8.0\ \mu\text{m}$ , caused by the emission of Polycyclic Aromatic Hydrocarbons (PAHs), excited by ultraviolet radiation (UV), which surrounds a region of ionized gas (Churchwell et al. 2006, 2007).

<sup>1</sup>Galactic Legacy Infrared Mid-Plane Survey Extraordinaire

The bubbles were detected in observations performed by the Spitzer satellite, in a survey that revealed about 600 bright objects at mid-infrared wavelengths (Churchwell et al. 2006). Shortly afterwards the Churchwell catalog were complemented by the Milky Way Project (MWP) catalog by Simpson et al. (2012). This is the most recent scientific citizen-generated catalog, where the bubbles were identified by thousands of volunteers and therefore their classification is more reliable. Deharveng et al. (2010) have identified and studied a large sample of bubbles and concluded that the shell of each one, detected at  $8.0\ \mu\text{m}$ , is an evidence of an HII region produced by the ionizing massive stars. Thompson et al. (2012) suggested that the expansion of the bubbles triggers the formation of Young Stellar Objects (YSOs) which is a non-negligible process in Galactic scales. Kendrew et al. (2012, 2016) also have observed this behavior and, although evidences of triggering via bubble expansion were missing, these authors found populations of YSOs near the borders of expanding bubbles, which could offer us important clues to the star formation process and the expansion of infrared bubbles.

We can interpret these bubbles as basically ionized gas surrounded by cold dust. A Photon-Dominated Region (PDR) in the inner regions of the shell, can be identified and described at mid-infrared wavelengths (Lefloch et al. 2005). The PDRs can be the result of the HII region expansion. They can be seen as regions where the ionization front is still progressing in the densest medium of the original cloud, generating an interface between ionized and neutral gases. The larger density in the PDR is possibly due to material collected by the expansion of the HII region. In this region the UV flux decreases sharply, allowing the existence of molecular and grain species. The massive stars interact with the original molecular cloud and, by their UV radiation, generate the interface between ionized gas and neutral gas.

In principle, the structure of the objects, should it be spherical shells or rings, allow us to understand correctly the kinematics of the gas and the chronology of the newly formed stars. Several works claimed that there was evidence for star formation triggered by the expansion of the HII region (Dewangan et al. 2012; Zavagno et al. 2010; Beuther et al. 2011). Yuan et al. (2014) found velocity differences of the order of  $30\ \text{km s}^{-1}$  between distinct parts of the ring in the bubble N6, which would indicate a quite larger expansion ve-

locity than those considered by other authors, of a few  $\text{km s}^{-1}$  (e.g. Beaumont & Williams 2010). Dale et al. (2005) and Dale & Bonnell (2008) carried out simulations to study the effects of stellar feedback in molecular clouds. They suggested that it is not possible to determine if the formation of an YSO was triggered or not by the expansion of the HII region and as a consequence studies of triggered star formation should be done statistically.

Therefore, it is important to gather a number of well studied bubbles to establish if they have similar formation histories, if they have similar morphology and if they give similar answers to the process about triggered star formation.

In this work we present a detailed study of N10, a remarkable bubble which has molecular clumps and YSOs associated with its surrounding shell. We present our CO observations and we analyze them together with the relevant data at different wavelengths:  $8.0\ \mu\text{m}$ , PAH emission;  $24\ \mu\text{m}$ , hot grains from ionized region;  $870\ \mu\text{m}$ , dust emission; and  $20\ \text{cm}$  free-free emission, from hot gas.

This paper is organized as follows: our target object is introduced in Section 2. In Section 3 we describe the CO observations and the archival data used in this paper. We dedicate the Section 4 to present our results and the Section 5 to discuss these results. Finally, we summarized our mainly conclusions in Section 6.

## 2. The bubble N10

N10 is situated in the direction  $l = 13.188^\circ$ ,  $b = 0.039^\circ$  (Churchwell et al. 2006). This object is also identified as MWP1G013189+000428 by Simpson et al. (2012). It appears in the Spitzer-GLIMPSE  $8.0\ \mu\text{m}$  image as a bright ring-like structure (Figure 1). The  $8.0\ \mu\text{m}$  emission in the border of bubbles is attributed to PDRs containing PAHs; the gas density in the PDR can be much larger (up to a factor 10) than that of the surrounding medium (Deharveng et al. 2010; Churchwell et al. 2006). In Figure 1 we show an ellipse to mark the boundaries of the bubble, for later reference in images at different wavelengths. Churchwell et al. (2006) consider N10 a bipolar (or double) bubble, since a small bubble (N11) seems to be connected to N10 in the North of it. However, Deharveng et al. (2015) recently showed that N10/N11 is not a bipolar bubble, as Churchwell et al. (2006) misidentified. In this work we deal only with the case of N10.

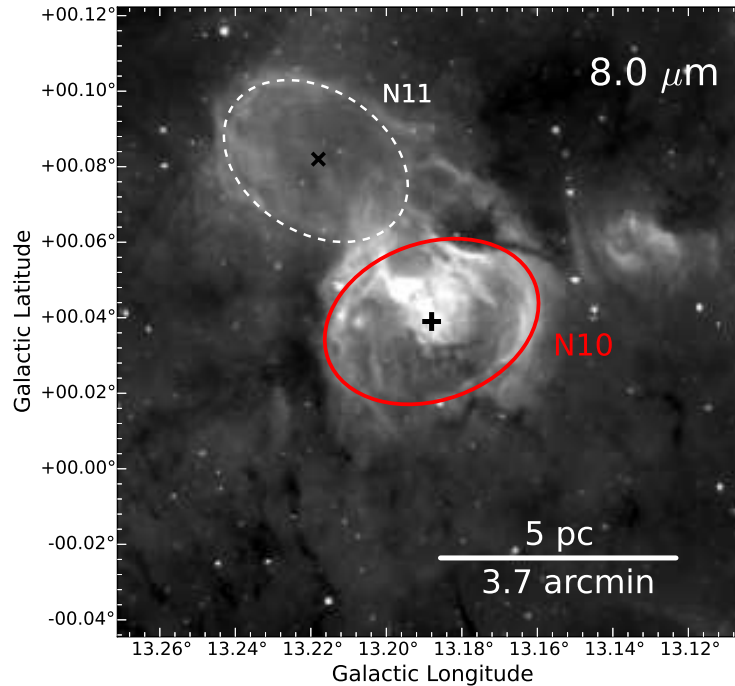


Fig. 1.— Map of the bubble N10, located to a distance of 4.7 kpc, at  $8.0 \mu\text{m}$ . The black cross indicates the center of the HII region inside the bubble of our interest. The red ellipse indicates the edge of N10. The scale corresponds to a field of 5 pc ( $\sim 3.7''$ ). The white dashed ellipse indicates N11 position, which center is located at  $l=13.218^\circ$ ,  $b=0.082^\circ$ , marked by the black “x”.

The distance of N10 was estimated as 4.9 kpc by Churchwell et al. (2006), 4.1 kpc by Beaumont & Williams (2010), 4.6 kpc by Pandian et al. (2008) and 4.9 kpc by Watson et al. (2008). These are kinematic distances estimated using different rotation curves, which explain the discrepancies.

A methanol ( $\text{CH}_3\text{OH}$ ) maser in N10 region was first reported by Szymczak et al. (2000), detected towards the IRAS 18111-1729 source. It is accepted that the methanol masers (as is the case of the present one) are associated with the earliest stages of massive star formation (Minier & Booth 2002). Figure 2 shows this methanol maser source located on the border of one of the two bright  $870 \mu\text{m}$  condensations adjacent to the bubble. The second  $\text{CH}_3\text{OH}$  maser reported by Pandian et al. (2008) seems to be associated with a SVSS<sup>2</sup> source.

In their study of the central region, Watson et al. (2008) identified four stars as possible ionizing stars

in N10 (see Table 1), based on their Spectral Energy Distributions (SEDs) which are well-fitted by a stellar photosphere. The position of stars are also plotted in Figure 2. Assuming a radius of 1.61 pc for the densest dark cloud, Ma et al. (2013) estimated a dynamical age  $t_{\text{dyn}} = 9.17 \times 10^4 \text{ yr}$  for N10. Nevertheless, they argue that this value could be larger since the density of the true ambient where the stars originally were formed could be larger than they considered.

Hereafter we will adopt the position of N10 and the ellipse in Figure 2 as reference: top of the bubble (higher galactic latitude with the center as reference), bottom (lower galactic latitude), right (lower galactic longitude) and left (higher galactic longitude).

### 3. Observations and data

#### 3.1. CO observations

The observations were carried out with PMO (Purple Mountain Observatory) 13.7-m radio telescope in 2012 June. We observed the  $J = 1 - 0$  tran-

<sup>2</sup>NRAO VLA Sky Survey (Condon et al. 1998)

TABLE 1  
CANDIDATES IONIZING STARS IN N10 SYSTEM.

ID <sup>a</sup>	A.R. (J2000)	DEC (J2000)	Spectral Type	A <sub>V</sub>
IN10-1	18 14 06.343	-17 28 33.86	O7.5 V	7
IN10-2	18 14 04.771	-17 27 58.74	O6.5 V	7
IN10-3	18 14 07.104	-17 29 21.27	O6 V	5
IN10-4	18 14 06.666	-17 29 21.34	O7 V	8

<sup>a</sup>Identification by Watson et al. (2008)

sition of  $^{12}\text{CO}$  (115.27 GHz),  $^{13}\text{CO}$  (110.20 GHz) and  $\text{C}^{18}\text{O}$  (109.78 GHz). The On-The-Fly (OTF) observing mode was applied to map a  $21' \times 25'$  region centered at  $\alpha_{2000} = 18^{\text{h}}14^{\text{m}}01^{\text{s}}.361$  and  $\delta_{2000} = -17^{\circ}28'23''.14$ . For the 13.7-m PMO antenna, we have considered a Half Power Beam Width (HPBW) around  $52''$ .

We used a 9 beam array of SIS receivers at the front end (Shan et al. 2012). The main beam efficiency at the center of the  $3 \times 3$  array is about 0.44 at 115 GHz and 0.48 at 110 GHz. Our spectral resolution was about 61 kHz, corresponding to velocity resolutions of  $0.16 \text{ km s}^{-1}$  (at 115 GHz) and  $0.17 \text{ km s}^{-1}$  (at 110 GHz and 109 GHz).

The cloudy weather condition during our observations led to system temperatures reaching 550 K and 350 K at 115 GHz and 110 GHz, respectively. This resulted in rms noises of 1.7 K and 1.2 K in the brightness temperature for  $^{12}\text{CO } J = 1 - 0$  and  $^{13}\text{CO } J = 1 - 0$ , respectively. Such large noise would make relatively weak signals undetectable. However, regions with strong line emission can be validly probed. The velocity information provided by these data convincingly reveal the kinematics of the bubble and molecular conditions in some subregions.

### 3.2. Other observations

Public data from infrared to centimeter surveys was used to analyze the bubble N10 at other wavelengths. The GLIMPSE survey (Benjamin et al. 2003) mapped parts of the inner Galactic plane, with IRAC (Infrared Array Camera; Fazio et al. 2004) on Spitzer Space Telescope. We obtained images of 4.5, 5.8 and 8.0  $\mu\text{m}$  IRAC bands Figure 3. The 24  $\mu\text{m}$  image of N10 was obtained from another survey of the inner Galactic plane, MIPS GAL, using the MIPS instrument (Multi-

band Imaging Photometer for the Spitzer; Rieke et al. 2004). In the panel at 24  $\mu\text{m}$  of Figure 3 we can see that this emission fills the whole area indicated by the red ellipse. This emission, typical of galactic bubbles, is caused by warm dust present in the region of ionized gas.

The existence of an HII region inside the bubble is confirmed by the radio continuum emission at 20 cm from MAGPIS (Helfand et al. 2006). In order to improve the continuum emission data, MAGPIS combined VLA images with images from a 1.4 GHz survey carried out by Reich et al. (1990) using the Effelsberg 100-m telescope. This emission, due to free-free process, is a good tracer of ionized gas.

N10 was mapped at sub-mm wavelengths with the APEX telescope (Miettinen 2012). The images at 870  $\mu\text{m}$  wavelength were obtained with ATLASGAL (APEX Telescope Large Area Survey of the Galaxy), an observing program using the LABOCA (Large Apex Bolometer Camera instrument Schuller et al. 2009). The 870  $\mu\text{m}$  cold dust emission is useful to reveal the presence of dense dark clouds. Two of these clouds, reported by Wienen et al. (2012), are seen bordering the bubble, along the upper and left borders of the bubble. The HII region, which is probably expanding, seems to be interacting with these clouds. We used the MAGPIS website<sup>3</sup> to obtain the images presented Figure 3.

We also used the all-sky Wide-Field Infrared Survey Explorer satellite (WISE; Wright et al. 2010) data to analyze the content of young stellar objects in N10, in order to reveal the regions where star formation took place recently and possible gradients of evolutionary stage.

<sup>3</sup><http://third.ucllnl.org/gps>

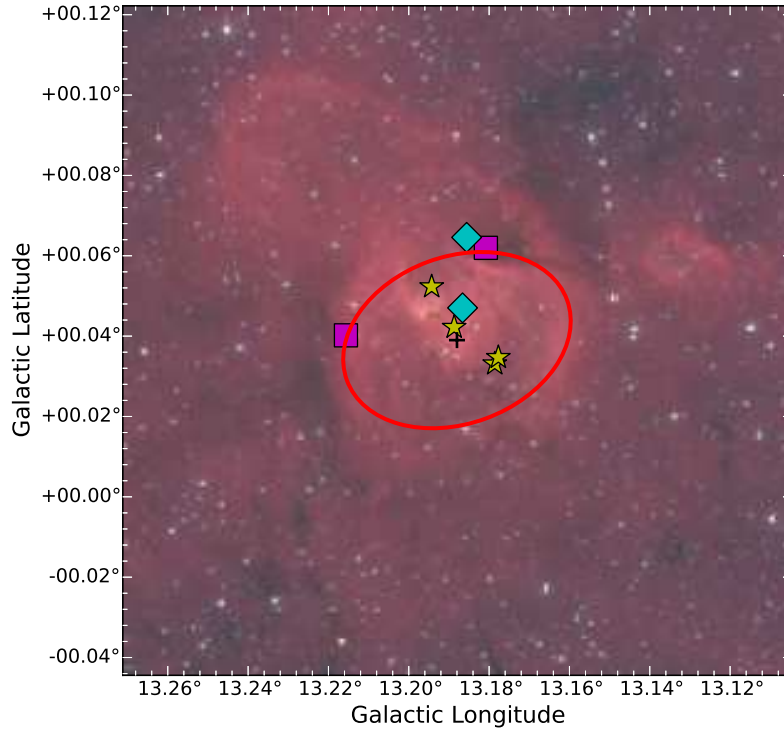


Fig. 2.— Three color composite image of bubble N10 with Spitzer-GLIMPSE 3.6  $\mu\text{m}$  (blue), 4.5  $\mu\text{m}$  (green) and 8.0  $\mu\text{m}$  (red). The positions of the stars from Watson et al. (2008) are marked as yellow stars; dust condensations identified by Deharveng et al. (2010) are indicated by magenta squares (#1 at the right side, #2 at the left side); cyan diamonds represents the position of methanol masers by Szymczak (2000; up) and Pandian (2008; down).

## 4. Results

### 4.1. Molecular Emission

The emission of  $^{12}\text{CO}$ ,  $^{13}\text{CO}$  and  $\text{C}^{18}\text{O}$  J=1-0 was observed at the same time. Strong emission of  $^{12}\text{CO}$  and  $^{13}\text{CO}$  was observed; the emission of  $\text{C}^{18}\text{O}$  is weak and we do not analyze in this work. The Figure 4 presents the observed spectral lines.

Detected  $^{12}\text{CO}$  and  $^{13}\text{CO}$  emission allows us to identify three peaks of velocity: at 20, 37 and 52  $\text{km s}^{-1}$ , approximately. The central velocities and line widths were determined by Gaussian fits using the CLASS package (GILDAS software<sup>4</sup>). In this paper, velocities are referred to the local standard of rest ( $V_{\text{LSR}}$ ). Upper panel in Figure 5 displays a channel map of  $^{12}\text{CO}$  emission and bottom panel shows the channel map of  $^{13}\text{CO}$  emission. The background in

both figures shows 8.0  $\mu\text{m}$  emission. We have fitted the channels by increasing the velocity from 45 to 62  $\text{km s}^{-1}$ . There is an strong correlation between  $^{12}\text{CO}$  and  $^{13}\text{CO}$  emission, specially in the range 48-53  $\text{km s}^{-1}$ .

Broad CO component centered at 20  $\text{km s}^{-1}$  has the lower intensity of the three peaks. Component centered at 37  $\text{km s}^{-1}$  presents narrower profile than the former, and lower intensity if compared with the component centered at 52  $\text{km s}^{-1}$ .

The velocities found in the literature for different emission lines associated with N10 range from 48.5 to 54.1  $\text{km s}^{-1}$ , as shown in Table 2. This leads us to adopt the component with peak at 52.6  $\text{km s}^{-1}$  as the one related to the source.

In our observation, velocities along the emission with peak at 52.6  $\text{km s}^{-1}$  range from 48 to 53  $\text{km s}^{-1}$ . In order to verify the correspondence between the physical distribution of molecular gas and the bubble

<sup>4</sup><http://www.iram.fr/IRAMFR/GILDAS>



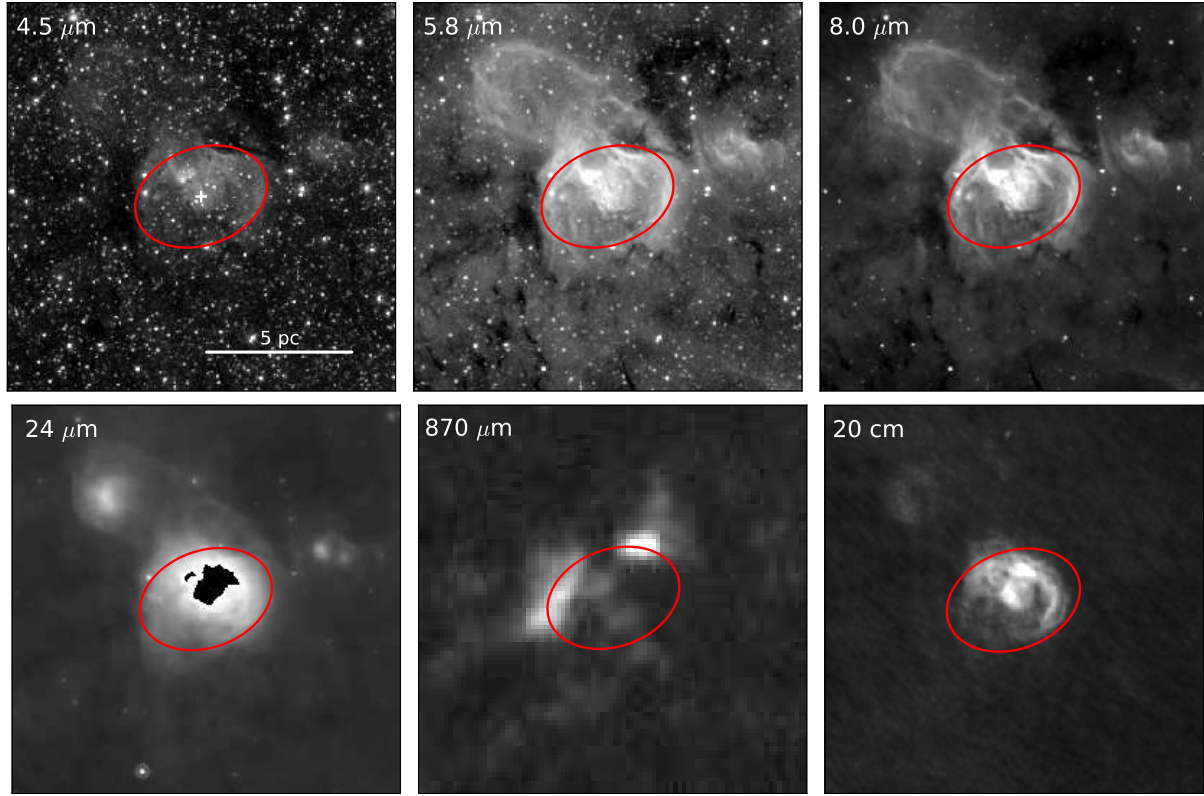


Fig. 3.— Multi-wavelength images of the N10 region. The panels show 4.5  $\mu\text{m}$ , 5.8  $\mu\text{m}$ , 8.0  $\mu\text{m}$ , 24  $\mu\text{m}$ , 870  $\mu\text{m}$  and 20 cm emission towards the target region, from Spitzer-GLIMPSE, Spitzer-MIPSGAL, LABOCA-ATLASGAL and GPS-VLA, respectively. All the images are showing the same region in the sky; in the first panel, white cross marks the center of the HII region; in all images the red ellipse is for reference, as shown in Figure 1.

seen in infrared,  $^{12}\text{CO}$  and  $^{13}\text{CO}$  contours of narrow-velocity emission were superposed over a Spitzer 8.0  $\mu\text{m}$  image in Figure 6. Spatial distribution of  $^{12}\text{CO}$  shows two main structures that seem to be related to the 8.0  $\mu\text{m}$  emission, and  $^{13}\text{CO}$  presents two denser clumps in the border of the ring morphology of N10, at the same position of  $^{12}\text{CO}$  structures.

#### 4.2. Distribution of gas and dust

We have studied the bubble N10 through the emission of the CO and the cold dust, which is useful to reveal the densest and coldest regions of N10. However, it is necessary to explore other tracers.

##### *Ionized gas*

Ionized gas associated with N10 can be traced by VLA 20 cm emission. The presence of emission at

$\nu = 1.5$  GHz implies that the HII region in the inner part of the bubble is created by UV photons. Using the Greg/GILDAS software we estimated the 20 cm total flux  $F_{20\text{ cm}} = 1.17$  Jy inside the bubble and we calculated the electron density ( $n_e$ ) according Panagia & Walmsley (1978):

$$\frac{n_e}{\text{cm}^{-3}} = 3.113 \times 10^2 \left( \frac{T_e}{10^4 \text{ K}} \right)^{0.25} \left( \frac{S_\nu}{\text{Jy}} \right)^{0.5} \left( \frac{D}{\text{kpc}} \right)^{-0.5} \times b(\nu, T)^{-0.5} \times \theta_R^{-1.5}, \quad (1)$$

where  $T_e$  in K is the electron temperature,  $S_\nu$  is the measured total flux density in Jy,  $D$  is the distance in kpc and  $\theta_R$  is the angular radius in arcmin. The function  $b(\nu, T)$  is defined as:

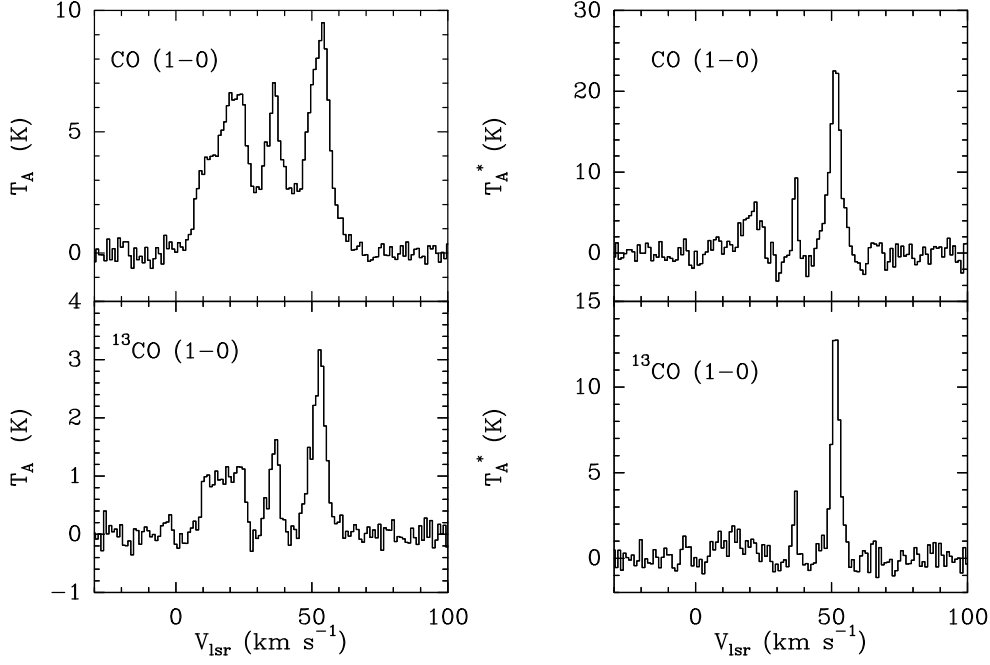


Fig. 4.— Spectral lines. The left column shows the average spectra of  $J = 1 - 0$  transition of  $^{12}\text{CO}$  in the upper panel and  $^{13}\text{CO}$  in the lower panel of the observed region ( $\Delta l = 0.002^\circ$ ,  $\Delta b = 0.304^\circ$ ). The right column presents spectra of these two lines in the peak position, at  $l = 13.21^\circ$ ,  $b = 0.037^\circ$ .

$$b(\nu, T) = 1 + 0.3195 \log \left( \frac{T_e}{10^4 \text{ K}} \right) - 0.2130 \log \left( \frac{\nu}{1 \text{ GHz}} \right). \quad (2)$$

Assuming  $T_e = 10^4 \text{ K}$  for the free-free emission region, the electron density is  $n_e = 129.71 \text{ cm}^{-3}$ .

Figure 7 displays two peaks of radio continuum emission in grayscale and black contours in left panel. In the same figure, right panel shows one of the peaks coinciding with an O-type star.

The number of Lyman continuum photons that are absorbed by the gas in the region HII was calculated using the radio continuum map, following the relation given by Matsakis et al. (1976):

$$N_{uv} = 7.5 \times 10^{46} \left( \frac{\nu}{\text{GHz}} \right)^{0.1} \left( \frac{T_e}{10^4 \text{ K}} \right)^{-0.45} \left( \frac{S_\nu}{\text{Jy}} \right) \left( \frac{D}{\text{kpc}} \right)^2 \quad (3)$$

We estimate  $N_{uv} = 1.86 \times 10^{49}$  ionizing photons  $\text{s}^{-1}$

in Lyman continuum, equivalent to a single star type O (Watson et al. 2008). Considering a model of H II region in expansion the neutral material accumulates between the ionization front and the shock front (Deharveng et al. 2010), the ionized gas is surrounded by a shell of dense, neutral material hosting PAHs, the main responsible of  $8.0 \mu\text{m}$  emission in infrared wavelengths. Therefore ionized gas appears confined by the bubble shell exhibited by  $8.0 \mu\text{m}$  emission in red color.

#### Cold and warm dust

In Figure 3 it has been displayed the set of emission maps at  $4.5$ ,  $5.8$ ,  $8.0$  and  $24 \mu\text{m}$ . These emissions, corresponding to warm dust, allows to identify clearly the expanding HII region around the bubble N10. The upper panels, maps at  $4.5$ ,  $5.8$  and  $8.0 \mu\text{m}$ , reveals the arc-shaped boarder of N10.

The thermal emission from cold dust is responsible for mainly continuum  $870 \mu\text{m}$  distribution towards N10, while the emission at  $8.0 \mu\text{m}$  originates by polycyclic aromatic hydrocarbons (PAHs) excited by UV photons. Figure 8 displays the emission at  $870 \mu\text{m}$  in grayscale and contours for N10 (left panel), and the

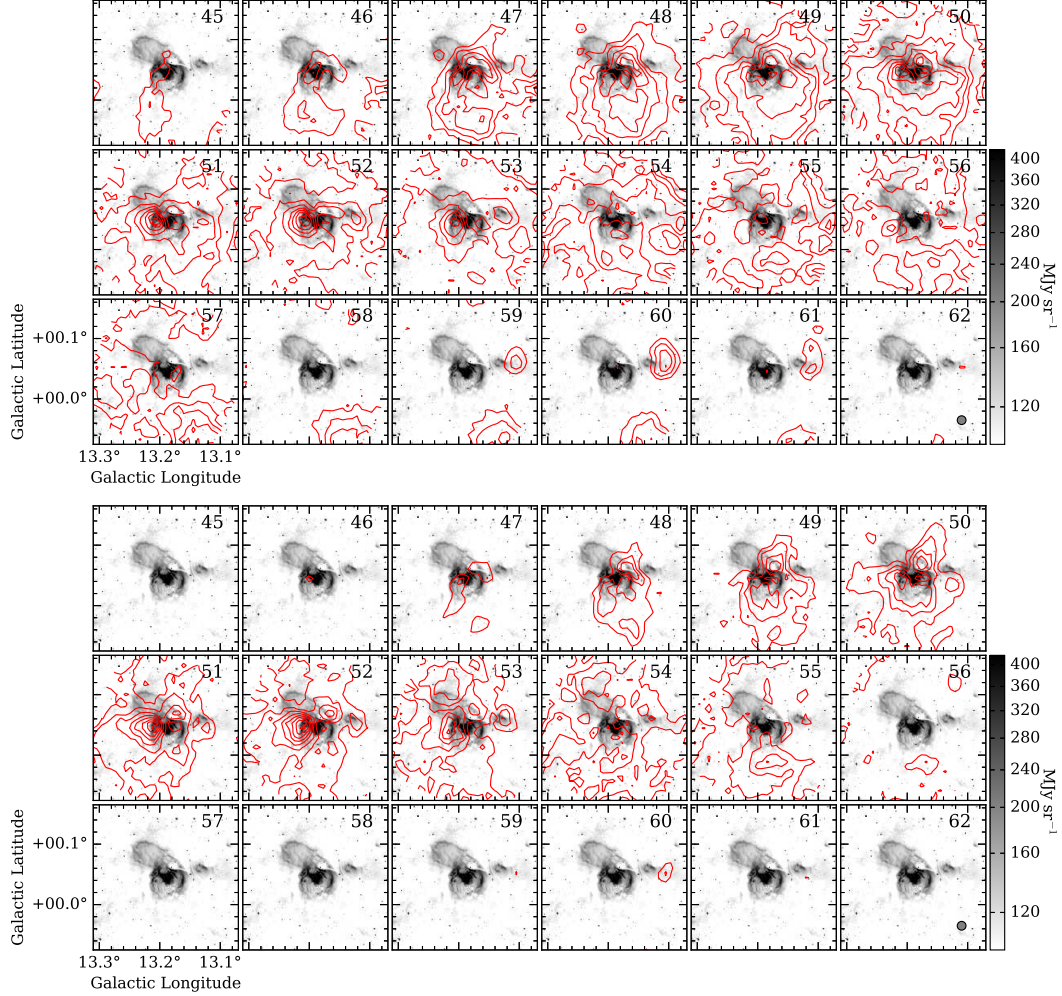


Fig. 5.— *Upper panel*: Channel maps of  $^{12}\text{CO}$   $J = 1-0$  emission in contours superimposed on the Spitzer  $8\,\mu\text{m}$  image. The contours start from  $5\,\sigma$  with steps of  $3\,\sigma$  ( $1\,\sigma = 0.90\,\text{K km s}^{-1}$ ). The main velocity in  $\text{km s}^{-1}$  is indicated in the left-upper corner of each panel. The small circle represents the beam size of  $^{12}\text{CO}$  observations. *Lower panel*: The same, for  $^{13}\text{CO}$   $J = 1-0$  emission. The contours start from  $5\,\sigma$  increasing with a step of  $3\,\sigma$  ( $1\,\sigma = 0.55\,\text{K km s}^{-1}$ ). The scale bar shows the  $8\,\mu$  flux intensity on a logarithmic scale and the small circle represents the beam size of  $^{13}\text{CO}$  observations.



TABLE 2  
VELOCITIES DERIVED TOWARDS THE BUBBLE N10.

Velocity	Method	Reference
$54.1 \text{ km s}^{-1}$	H II region, radio recombination line	1
$48.5 \text{ km s}^{-1}$	6.7 GHz methanol maser emission	2
$54.1 \text{ km s}^{-1}$	HI absorption line	3
$50.2 \text{ km s}^{-1}$	CO line emission	4
$48.5 \text{ km s}^{-1}$	NH <sub>3</sub> inversion line (from $870 \mu\text{m}$ data)	5
$54.1 \text{ km s}^{-1}$	mid-infrared from WISE HII region	6

References. — (1) Lockman 1989; (2) Szymczak et al. 2000; (3) Pandian et al. 2008; (4) Beaumont & Williams 2010; (5) Wienen et al. 2012; (6) Anderson et al. 2014.

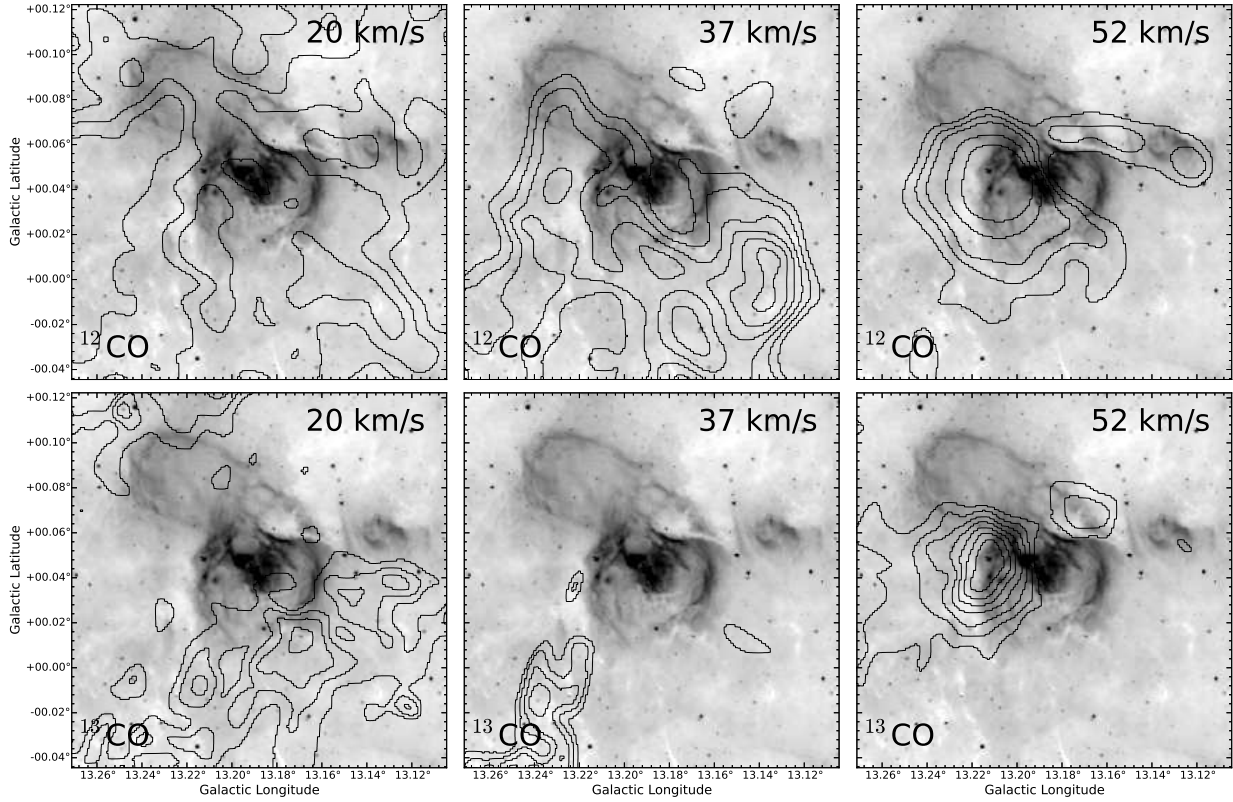


Fig. 6.— The upper panels show contours of  $^{12}\text{CO}$  emission distribution centered at  $20 \text{ km s}^{-1}$  from 6 to 13-K in steps of 1-K (*left*); at  $37 \text{ km s}^{-1}$  in steps of 1-K, from 8 to 14-K (*middle*); at  $52 \text{ km s}^{-1}$  from 5 to 12-K, in steps of 1-K (*right*). The lower panels display contours of  $^{13}\text{CO}$  emission distribution centered at  $20 \text{ km s}^{-1}$  from 1 to 3-K in steps of 0.5-K (*left*); at  $37 \text{ km s}^{-1}$  in steps of 1-K, from 5 to 10-K (*middle*); at  $52 \text{ km s}^{-1}$  from 10 to 21-K, in steps of 1-K (*right*). All panels exhibit  $8.0 \mu\text{m}$  image in background.

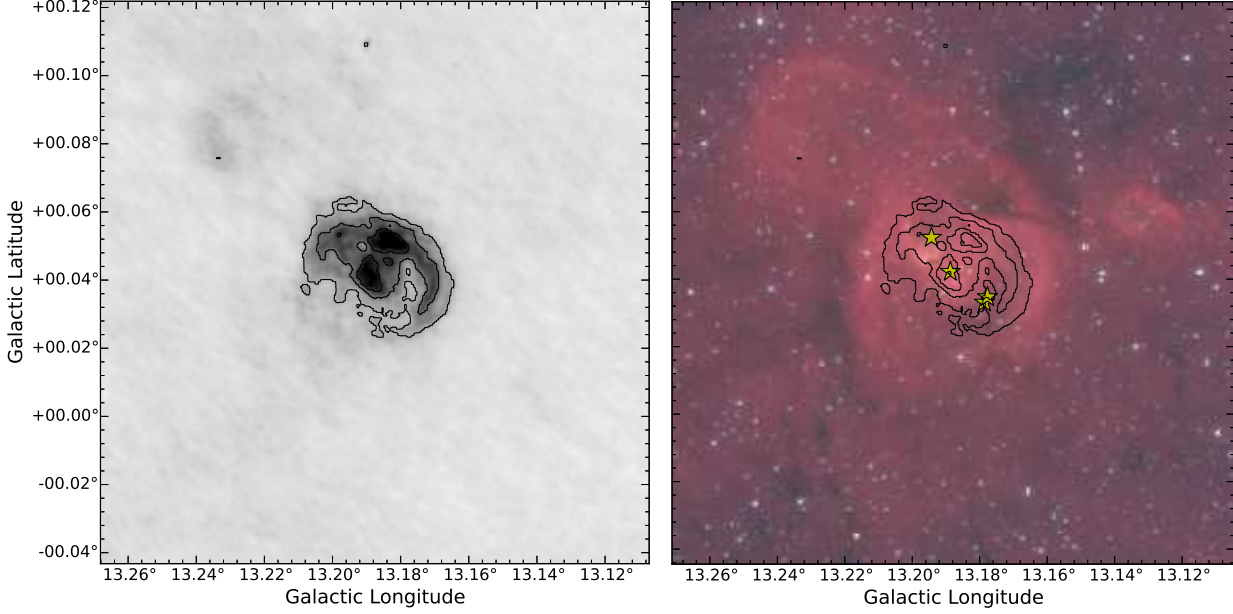


Fig. 7.— *Left panel*: VLA 20 cm (1.4 GHz) intensity in grayscale, from 0 to 20 mJy beam<sup>-1</sup>, with contours start from 2  $\sigma$  with steps of 2  $\sigma$  (1  $\sigma$  = 2.8 mJy beam<sup>-1</sup>). *Right panel*: RGB Spitzer image in background (3.6  $\mu$ m in blue, 4.5  $\mu$ m in green and 8.0  $\mu$ m in red). Yellow stars marks the position of the candidates ionizing stars.

same contours of the cold dust emission are superimposed on an Spitzer 8.0  $\mu$ m image (right panel).

The two 870  $\mu$ m clumps coincide with <sup>13</sup>CO molecular condensations detected at the peak velocity of 52 km s<sup>-1</sup> shown in upper right panel Figure 6. According Dewangan et al. (2015) the coincidence of distribution of the molecular gas, PAH and cold dust emission are an evidence of star-forming material around the bubble. We calculated the physical parameters for the denser condensation in the right of the Figure 8. We here consider that the 870  $\mu$ m radiation originates from the thermal radiation from dust grains. The total mass (dust and gas) in grams can be estimated following relation by Hildebrand (1983):

$$M_{\text{tot}} = 100 \frac{S_{870\mu\text{m}} D^2}{\kappa_{870\mu\text{m}} B_{870\mu\text{m}}(T_{\text{dust}})}, \quad (4)$$

where  $S_{870\mu\text{m}}$  is the flux density of 870  $\mu$ m emission in Jy,  $\kappa_{870\mu\text{m}}$  is the dust opacity per unity mass at 870  $\mu$ m and  $B_{870\mu\text{m}}$  is the Planck function for a given dust temperature  $T_{\text{dust}}$  in Jy. We assumed  $T_{\text{dust}} = 20$  K and  $\kappa_{870\mu\text{m}} = 1.8$  cm<sup>2</sup> g<sup>-1</sup>. We assumed a gas-to-dust ratio of 100 (Mathis et al. 1977; Draine & Anderson 1985).

We can calculate the  $H_2$  column density  $N(H_2)$  using the following formula, by Deharveng et al. (2010):

$$N(H_2) = \frac{100 F_{870\mu\text{m}}}{\kappa_{870\mu\text{m}} B_{870\mu\text{m}}(T_{\text{dust}}) 2.8 m_H \Omega_{\text{beam}}}, \quad (5)$$

where  $N(H_2)$  is in cm<sup>-2</sup>, the surface brightness  $F_{870\mu\text{m}}$  is in Jy beam<sup>-1</sup>, the beam solid angle  $\Omega_{\text{beam}}$  is in steradians and the hydrogen mass  $m_H$  is in grams.

We calculate the effective radius of the clumps as:

$$R_D = \left( \frac{\theta_{\text{maj},D}}{2} \times \frac{\theta_{\text{min},D}}{2} \right)^{0.5}, \quad (6)$$

where the major and minor deconvolved FWHM of the condensation ( $\theta_{\text{maj},D}$  and  $\theta_{\text{min},D}$ ) was calculated as:

$$\theta_{\text{maj},D} = \sqrt{\theta_{\text{maj}}^2 - \theta_{\text{HPBW}}^2}, \quad \theta_{\text{min},D} = \sqrt{\theta_{\text{min}}^2 - \theta_{\text{HPBW}}^2} \quad (7)$$

where  $\theta_{\text{maj}}$  and  $\theta_{\text{min}}$  are the major and the minor FWHM sizes, respectively, was obtained by using the

GreG/GILDAS fitting. We found that  $\theta_{maj} = 44$  arcsec and  $\theta_{min} = 32$  arcsec. The half-power beamwidth for  $870 \mu m$  is  $\theta_{HPBW} = 19.2$  arcsec. Therefore,  $R_{min,D} = 25.6$  arcsec and  $R_{maj,D} = 39.6$  arcsec (0.6 pc and 0.9 pc, respectively, at a distance of 4.7 kpc). According to Equation 6 the mean radius deconvolved is  $R_D = 0.36$  pc, at a distance 4.7 kpc.

The average volume density for this condensation, assuming a spherical geometry, was calculated according Duronea et al. (2015):

$$n(H_2) = \frac{M_{tot}}{4/3 \pi R_D^3 \mu m_H}, \quad (8)$$

where  $\mu$  is the mean molecular weight and  $m_H$  is the mass of hydrogen atom. We assumed  $\mu = 2.33$  g and  $m_H = 1.67 \times 10^{-24}$  g.

In short, we found a column density  $N(H_2) = 6.3 \times 10^{22} \text{ cm}^{-2}$ , a total mass  $M_{tot} = 240 M_\odot$ , the mean radius deconvolved is  $R_D = 0.36$  pc and the average volume density is  $n(H_2) = 9.4 \times 10^4 \text{ cm}^{-3}$ .

Warm dust can also be traced in this region by distribution of  $24 \mu m$  emission in grayscale. VLA 20 cm emission is shown in contours. Warm dust and ionized emissions appears to be quite correlated as Figure 9 displays, as expected for HII regions (e.g. Paladini et al. 2012).

We can notice that the IRAC  $24 \mu m$  emission appears saturated close to the VLA 20 cm emission. This wavelength band concerns dust and gas ionized emission, which is shown in our results too. From Figure 3 we can see that the saturated region is that both the IRAC and 20cm emissions are strong.

In resume, the map at  $8.0 \mu m$  is very useful, since it traces the expanding arc in the upper left part of N10, this region is associated with ionized gas, excited PAHs and warm dust.

On the other hand, the emission map at 20 cm exposes the central part of the HII region that is surrounded by the N10 boarder; as would be expected, this region contains dust warmer than the expanding arcs. Furthermore, Figure 7 shows clearly the central part of the HII region.

#### 4.3. Distance

Adopting a distance of 4.6 kpc from Pandian et al. (2008) (see also Deharveng et al. 2010), the physical size of the ring is about  $4.7 \times 2.5$  pc. Using this distance, N10 is found to be close to the near extremity

of the Galactic bar, a region of intensive star formation (see e.g. the maps of the Galactic arms structure by Hou & Han 2014).

For this work, using circular Galactic rotation models (e.g. Brand & Blitz 1993) is possible to compute near and far kinematic distances of the source; we have analyzed the kinematic distance ambiguity (KDA) and results shows the near kinematic one may be more reasonable.

Churchwell et al. (2006) argued that infrared bubbles are more likely located at their near kinematic distances, since objects on the far side of the Galactic disk would be obscured by interstellar extinction and contamination of other structures.

Based on our CO observations and using the velocity of  $52.6 \text{ km s}^{-1}$  (see Subsection 4.4), we obtained near and far kinematic distances of 4.7 kpc and 11.3 kpc, respectively. This value is compatible with the near distance estimated by Szymczak et al. (2000)  $d = 4.4$  kpc, using the methanol maser emission (see Table 2). Since N10 is located in the inner disk of the Galaxy, we adopt a 10% uncertainty for the kinematic distance (Yuan et al. 2014), resulting in the value of  $4.7 \pm 0.5$  kpc for N10.

#### 4.4. Observed and derived parameters

In the following discussion we adopt the labels given in Figure 10 to refer to identified condensations. Due to the poor spatial resolution of PMO (the beam size is  $\sim 0.9$  pc in our observations), the sizes of these molecular condensations could be smaller than 0.9 pc.

We used CLASS to calculate the parameters performing Gaussian fits to the average spectra obtained for the whole observed region. We obtained the centroid velocity ( $V_{LSR}$ ), the antenna temperature ( $T_A^*$ ), and the full width at half-maximum ( $\Delta V_{FWHM}$ ). These observed parameters are shown in Table 3.

In order to understand the evolutionary status of molecular clumps, we derived the physical properties for the two clumps we identified in our CO observations. The mass of the clumps were estimated by using the Miriad software package (Sault et al. 1995).

The mass of the molecular gas in a clump is calculated from the intensity of the emission line, under the local thermal equilibrium (LTE) assumption. With the radiation transfer equation Garden et al. (1991) we derived the mass of the clumps under LTE condition, as follow:

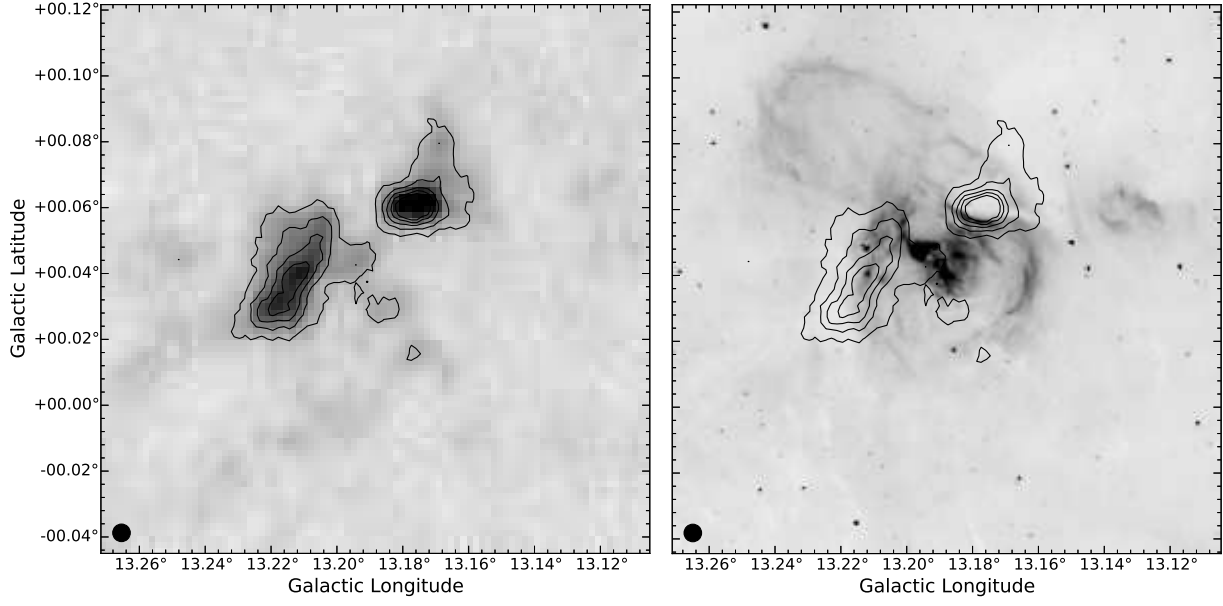


Fig. 8.— *Left panel:* LABOCA 870  $\mu\text{m}$  emission showing the distribution of cold dust in grayscale, from 0 to 5 Jy beam<sup>-1</sup>, with contours starting from 1  $\sigma$  to 5  $\sigma$ , in steps of 1  $\sigma$  (1  $\sigma$  = 0.5 Jy beam<sup>-1</sup>). *Right panel:* Spitzer 8.0  $\mu\text{m}$  image in background, overlaid with the same 870  $\mu\text{m}$  contours of left figure. In both figures the black dot represents the beam size.

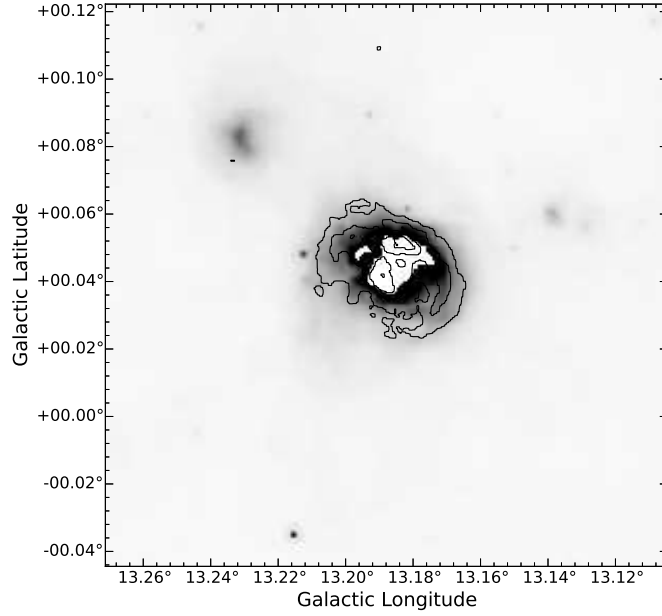


Fig. 9.— 24  $\mu\text{m}$  distribution in grayscale from 0 to 2280 MJy sr<sup>-1</sup> with the same 20 cm contours of left panel in Figure 7.

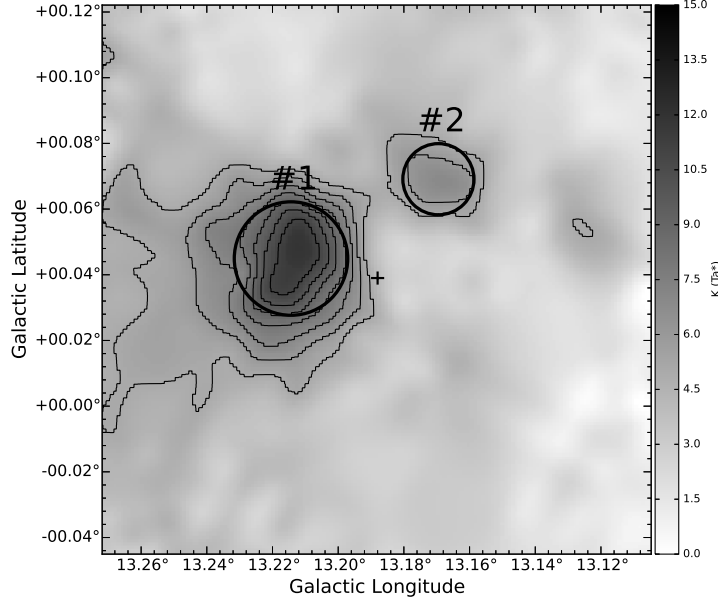


Fig. 10.— Region of the clumps identified in  $^{13}\text{CO}$  intensity centered at  $52 \text{ km s}^{-1}$ , in grayscale. Clump #1 and Clump #2 seem to be physically associated with bubble N10. Black contours show also  $^{13}\text{CO}$  emission from 5 to 11-K, in steps of 1-K. The black cross indicates the center of the HII region inside N10.

$$M_{\text{LTE}} = \frac{4}{3} \pi R^3 m_{\text{H}_2} \mu_g n_{\text{H}_2} \quad (9)$$

where  $M_{\text{LTE}}$  is given in solar masses  $M_{\odot}$ ,  $m_{\text{H}_2}$  is the mass of hydrogen molecule,  $\mu_g = 1.36$  is the mean atomic weight of the gas and  $n_{\text{H}_2} = N/2R$  is the volume density. The mean radius of the clump is obtained by the relation  $R = \sqrt{b_{\text{maj}} \times b_{\text{min}}}/2$ , where  $b_{\text{maj}}$  and  $b_{\text{min}}$  are the sizes of the minor and major axes of the ellipse, respectively, obtained using the Miriad software.

We first estimated the value of the column density  $H_2$  through the CO column density. According to Garden et al. (1991) the column density  $N$  of a rigid, asymmetric linear molecule, under LTE condition, can be expressed by:

$$N = \frac{3k}{8\pi^3 B \mu^2} \times \frac{\exp[h B J(J+1)/k T_{\text{ex}}]}{(J+1)} \times \frac{(T_{\text{ex}} + hB/3k)}{[1 - \exp(-h\nu/kT_{\text{ex}})]} \times \int \tau dv \quad (10)$$

where  $B$  is the rotational constant,  $J$  is the rotational quantum number of the lower state of the observed

transition and  $\mu$  is the electric dipole of the molecule.  $T_{\text{ex}}$  is the excitation temperature and  $\tau$  is the optical depth from 48 to  $53 \text{ km s}^{-1}$ .

Since the excitation temperature ( $T_{\text{ex}}$ ) is measured as a function of brightness temperature ( $T_r$ ), we estimate (Garden et al. 1991):

$$T_r = \frac{h\nu}{k} \times \left[ \frac{1}{\exp(h\nu/kT_{\text{ex}}) - 1} - \frac{1}{\exp(h\nu/kT_{\text{bg}}) - 1} \right] \times [1 - \exp(-\tau)]f \quad (11)$$

where  $T_r$  is the brightness temperature and the temperature of the cosmic background radiation  $T_{\text{bg}} = 2.73 \text{ K}$ . Here we assume a filling factor of  $f = 1$ .

Assuming that  $T_{\text{ex}}$  is the same for  $^{12}\text{CO}$  and for  $^{13}\text{CO}$ , the optical depth for both lines can be obtained directly comparing the measure of its brightness temperatures  $T_r$  (Garden et al. 1991):

$$\frac{T_r(^{12}\text{CO})}{T_r(^{13}\text{CO})} \approx \frac{1 - \exp(-\tau_{12})}{1 - \exp(-\tau_{13})} \quad (12)$$

We adopted an isotope ratio of  $[^{12}\text{CO}]/[^{13}\text{CO}] = 60$



(Deharveng et al. 2008; Wilson & Rood 1994), implying  $\tau_{12}/\tau_{13} = 60$ , and the canonical  $[\text{CO}]/[\text{H}_2]$  abundance ratio of  $10^{-4}$ .

Thus we can estimate the optical depth from Equation 12, and then, using it in Equation 11, and knowing the brightness temperature, we can estimate  $T_{ex}$ .

Using the estimated value of  $T_{ex}$  for the line  $^{13}\text{CO}$ , we can finally obtain the hydrogen column density ( $N_{\text{H}_2}$ ) using the equation 10. Thus, the intensity of the  $^{13}\text{CO}$  line traces the column density of the clumps #1 and #2, as listed in Table 4.

Obtaining the velocity dispersion and the mass under LTE assumption we can estimate the virial condition, by comparing the gas mass ( $M_{\text{LTE}}$ ) with the virial mass ( $M_{\text{virial}}$ ). In a cloud in which the temporal average kinetic energy is equal to half of the temporal average of the potential energy, the system is considered in virial equilibrium. The assumption that a gravitationally bound system is in virial equilibrium is widely used in astrophysics to estimate its mass (Huang 1954). The virial mass  $M_{\text{virial}}$  is given by Ungerechts et al. (2000) by the expression:

$$\frac{M_{\text{virial}}}{M_{\odot}} = 2.10 \times 10^2 \left( \frac{R}{\text{pc}} \right) \left( \frac{\Delta V_{\text{FWHM}}}{\text{km s}^{-1}} \right)^2 \quad (13)$$

where  $R$  is the mean radius of the clump and  $\Delta V_{\text{FWHM}}$  is the line width of  $^{13}\text{CO}$  line.

The Jeans mass  $M_J$  is the mass above which a gas cloud will collapse, for a given density and temperature, when the gravitational attraction overcomes the pressure of the gas. It can be calculated according to Stahler & Palla (2005):

$$\frac{M_{\text{Jeans}}}{M_{\odot}} = \left( \frac{T}{10\text{K}} \right)^{3/2} \left( \frac{n_{\text{H}_2}}{10^4 \text{ cm}^{-3}} \right)^{-1/2} \quad (14)$$

The results are presented in Table 4 where the columns 2 – 7 list the following clump parameters: mean radius ( $R$ ), excitation temperature ( $T_{ex}$ ), column density ( $N_{\text{H}_2}$ ), volume density ( $n_{\text{H}_2}$ ), gas mass calculated under LTE assumption ( $M_{\text{LTE}}$ ), virial mass ( $M_{\text{virial}}$ ) and Jeans mass ( $M_{\text{Jeans}}$ ). We discuss the clump status in Subsection 5.1.

#### 4.5. Identification of YSOs in the field of N10

The distribution of Young Stellar Objects (YSOs) plays a major role in the interpretation of the dynamics

of star forming region. To identify the YSOs present in the field of N10, we adopted the method described by Koenig & Leisawitz (2014) (hereafter KL), based on the data of the Wide-field Infrared Survey Explorer (WISE; see Wright et al. 2010). In particular we used the AllWISE release (Cutri et al. 2011<sup>5</sup>, Cutri et al. 2013), which combined the data from the cryogenic and post-cryogenic phases of the survey, resulting in a catalog with enhanced sensitivity.

The catalog was accessed through the VIZIER facility of the Strasbourg Data Center. The catalog contains infrared photometric data at 3.6, 4.9, 5.8 and 22  $\mu\text{m}$  wavelengths, hereafter designated as w1, w2, w3 and w4 bands, respectively. In a first step, we selected all the objects situated in the area around N10 that we explored, in the range of Galactic coordinates  $13.11^\circ < l < 13.27^\circ$  and  $-0.04^\circ < b < 0.12^\circ$ .

We found 565 WISE sources in this area. We next filtered this list of sources by applying a serie of quality criteria defined by KL, that they call the uncertainty/signal-to-noise/chi-squared criteria. The purpose of this is to avoid regions in the space of these parameters with relatively high probability of spurious catalog entry. Accordingly, the Class I YSOs are classified as such if their color matches with all the following criteria:

$$\begin{aligned} w1 - w3 &> 2.0; \\ w1 - w2 &> -0.42 \times (w2 - w3) + 2.2; \\ w1 - w2 &> 0.46 \times (w1 - w3) - 0.9; \\ w2 - w3 &< 4.5. \end{aligned}$$

These conditions reflect the divisions in the SED slope  $\alpha = d \log(\lambda F_{\lambda}) / d \log \lambda$ .

The Class II objects were also classified according to KL, whose criteria are:

$$\begin{aligned} w1 - w2 &> 0.25; \\ w1 - w2 &< -0.9 \times (w2 - w3) + 0.25; \\ w1 - w2 &> 0.46 \times (w2 - w3) - 0.9; \\ w2 - w3 &< 4.5. \end{aligned}$$

For w3 we kept only the condition of S/N larger than 5. It is considered that if a source satisfies the

<sup>5</sup>Cutri & IPAC/WISE Science Data Center Team (2011)

TABLE 3

OBSERVED LINE PARAMETERS OBTAINED OVER THE INTEGRATED AREA DESCRIBED IN FIGURE 4, WHERE  $V_{lsr}$  IS THE CENTROID VELOCITY OF THE MAIN PEAK, THE  $T_A^*$  IS THE ANTENNA TEMPERATURE AND  $\Delta V_{FWHM}$  IS THE FULL WIDTH AT HALF-MAXIMUM OF LINES.

	$V_{lsr}$ (km s <sup>-1</sup> )	$T_A^*$ (K)	$\Delta V_{FWHM}$ (km s <sup>-1</sup> )
<sup>12</sup> CO	52.6	8.3	9.2
<sup>13</sup> CO	52.6	2.9	6.1

TABLE 4

DERIVED PARAMETERS OF THE CLUMPS OBSERVED IN <sup>13</sup>CO.

clump	R (pc)	$T_{ex}$ (K)	$N_{H_2}$ (10 <sup>22</sup> cm <sup>-2</sup> )	$n_{H_2}$ (10 <sup>3</sup> cm <sup>-3</sup> )	$M_{LTE}$ (10 <sup>3</sup> M <sub>⊙</sub> )	$M_{virial}$ (10 <sup>3</sup> M <sub>⊙</sub> )	$M_{Jeans}$ (10 <sup>3</sup> M <sub>⊙</sub> )
#1	1.1	16.8	4.1	4.2	2.6	9.3	7.0
#2	1.2	12.9	3.3	3.9	1.5	7.8	4.7

criteria of being a true source in any one of the bands, it has little probability of being a fake one and will be included in the final list. After this filtering the list of sources reduced to 407 entries.

Next step was to separate the sources into Class I, Class II, Transition Disks and remaining objects. Following KL, the Class I and Class II YSOs are classified as such, based on the w1-w2 versus w2-w3 color-color diagram only. The regions of the diagram that are used to classify the YSOs are defined by a number of frontier lines, shown in Figure 12. The equations of the lines are given by KL (their equations 12 to 20). We found 12 Class I stars and 91 Class II sources. The Transition Disk stars are selected separately by means of the w1-w2 versus w2-w3 color-color diagram as shown in Figure 13. We found 131 transition disk stars. Note that the selection criteria follow an order of priority: a Class I object will remain Class I even if it also satisfies the criterion for Class II, and next the Class II selection prevails over the following selection. This is why we find many Class II objects in the box defining transition disk stars in Figure 13: they were classified Class II in the previous step, on the basis of the different color-color plot.

This selection of Class I objects is robust, since these objects are well separated from the other classes in the color diagrams. Furthermore, we made experi-

ments with another classification scheme available in the literature (using Spitzer data, e.g. Gutermuth et al. 2009) and the same Class I objects were retrieved. On the other hand, the distinction between Class II and Transition Disk is a little arbitrary, as we can see some overlap in Figures 12 and 13. In the samples of objects previously known to belong to given classes, used by KL to decide the position of the frontier lines in Figures 12 and 13, one can see a number of transition disk sources in the locus of Class II and vice versa. So, one must consider that the decision to attribute sources to one or the other classes is only valid in a statistical sense, being correct in about 70% of the cases.

#### 4.6. SED fitting

We have compared the position of Class I YSOs, the most embedded young stellar sources, with the molecular distribution and the objects identified from #1 to #9 (see Table 6) are more likely to be physically related to N10 molecular structure. We have fitted their spectral energy distribution (SED) by using the online tool developed by Robitaille et al. (2007). Radiation transfer models were fitted to observational data extracted from WISE catalog based on a  $\chi^2$  test. We selected models for which  $\chi^2 - \chi_{min}^2 < 3n$ , where  $\chi_{min}^2$  is the minimum value and  $n$  is the number of input data.

The fitting was performed using fluxes from WISE

data, distance ranges from 4.23 to 5.17 kpc. Interstellar extinction in the direction of N10 was predicted to be approximately 10.7 mag according to model S of Amôres & Lépine (2005), values adopted were from 9.7 to 11.7 mag. The best fit are shown in Figure 11. Resulting values for model parameters are given in Table 5. We found that Class I YSOs have stellar mass ranging from  $\sim 1$  to  $\sim 13 M_{\odot}$ , stellar temperature  $\sim 4000 - 20000$  K, total luminosity  $\sim 3 \times 10^1 - 1 \times 10^3 L_{\odot}$ , envelope accretion rate  $\sim 9 \times 10^{-8} - 3 \times 10^{-3} M_{\odot} \text{ yr}^{-1}$ , disk mass  $\sim 7 \times 10^{-3} - 6 \times 10^{-1} M_{\odot}$  and stellar ages from  $\sim 2 \times 10^3$  to  $\sim 1 \times 10^6$  yr.

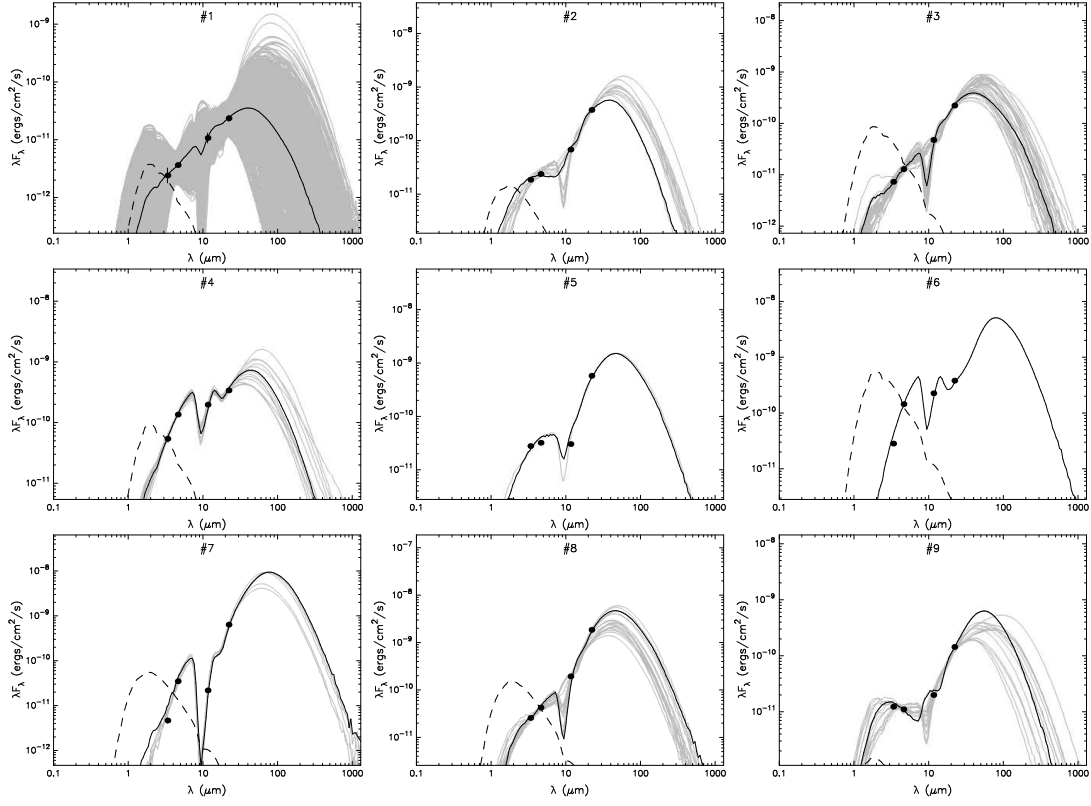


Fig. 11.— The filled circles show the input fluxes. The black line shows the best fit. The dashed line shows the stellar photosphere corresponding to the central source of the best fitting model, as it would look in the absence of circumstellar dust (but including interstellar extinction).

TABLE 5  
PHYSICAL PARAMETERS DERIVED FROM ROBITAILLE ET AL. (2007) MODEL, FOR ASSOCIATED CLASS I OBJECTS CANDIDATES.

Parameters	Class I YSOs <sup>a</sup>								
	1	2	3	4	5	6	7	8	9
Stellar Mass ( $M_{\odot}$ )	1.42	6.53	7.07	6.08	7.42	9.86	12.94	12.89	6.43
Stellar Temperature (K)	4173	10107	4293	4148	20167	4260	12262	7471	19400
Total Luminosity ( $L_{\odot}$ ) <sup>b</sup>	$3.11 \times 10^1$	$1.02 \times 10^3$	$5.45 \times 10^2$	$5.96 \times 10^2$	$2.33 \times 10^3$	$2.47 \times 10^3$	$1.13 \times 10^4$	$7.31 \times 10^3$	$1.19 \times 10^3$
$\dot{M}_{env}$ ( $M_{\odot} \text{ yr}^{-1}$ )	$2.49 \times 10^{-5}$	$1.20 \times 10^{-5}$	$4.70 \times 10^{-5}$	$1.19 \times 10^{-5}$	$7.60 \times 10^{-5}$	$1.12 \times 10^{-5}$	$3.61 \times 10^{-3}$	$2.25 \times 10^{-4}$	$8.62 \times 10^{-8}$
Disk Mass ( $M_{\odot}$ ) <sup>c</sup>	$1.01 \times 10^{-2}$	$3.05 \times 10^{-2}$	$3.38 \times 10^{-2}$	$4.45 \times 10^{-3}$	$1.46 \times 10^{-3}$	$7.71 \times 10^{-3}$	$1.49 \times 10^{-1}$	$6.09 \times 10^{-1}$	$5.25 \times 10^{-5}$
Stellar Age (yr)	$1.24 \times 10^4$	$2.77 \times 10^5$	$7.07 \times 10^3$	$1.84 \times 10^3$	$2.97 \times 10^5$	$2.41 \times 10^3$	$2.88 \times 10^4$	$1.60 \times 10^4$	$1.02 \times 10^6$

<sup>a</sup>Identification from Table 6

<sup>b</sup>Total system luminosity.

<sup>c</sup>Envelope and ambient density mass, in solar masses.



TABLE 6  
YOUNG STELLAR OBJECTS (YSO) CANDIDATES TOWARDS THE N10 REGION.

Candidate #	l [°]	b [°]	Identification	Fluxes [mag]				Classification
				[3.4]	[4.6]	[12]	[22]	
1	13.1141	0.0566	J181354.14-173204.6	12.651	11.220	7.212	4.212	Class I
2	13.1385	0.0593	J181356.48-173043.0	10.428	9.181	5.204	1.246	Class I
3	13.1383	0.0566	J181357.08-173048.2	11.451	9.848	5.595	1.771	Class I
4	13.2124	0.0402	J181409.60-172722.1	9.274	7.294	4.049	1.312	Class I
5	13.2007	0.0286	J181410.77-172819.3	9.995	8.855	6.081	0.734	Class I
6	13.2126	0.0477	J181407.98-172708.4	9.978	7.224	3.903	1.187	Class I
7	13.1818	0.0608	J181401.37-172823.3	11.937	8.766	6.442	0.629	Class I
8	13.2015	0.0554	J181404.94-172730.5	10.081	8.552	4.069	-0.537	Class I
9	13.2016	0.0681	J181402.15-172708.2	10.877	10.015	6.538	2.244	Class I
10	13.2155	-0.0350	J181426.60-172921.9	9.291	7.367	4.237	1.531	Class I
11	13.2396	-0.0057	J181423.03-172715.2	12.263	11.050	8.256	5.221	Class I
12	13.1931	0.0888	J181356.55-172659.5	12.308	10.741	6.260	3.168	Class I
13	13.1114	0.1134	J181341.27-173035.2	10.397	9.934	8.657	4.825	Class II
14	13.1135	-0.0134	J181409.56-173407.1	11.620	11.198	9.670	7.655	Class II
15	13.1389	-0.0279	J181415.81-173311.7	11.511	11.061	9.146	6.480	Class II
16	13.1384	-0.0162	J181413.16-173253.3	11.235	10.748	8.809	6.800	Class II
17	13.1147	-0.0195	J181411.06-173413.8	11.343	11.046	8.968	7.287	Class II
18	13.1449	-0.0193	J181414.65-173237.9	11.031	10.757	8.852	6.340	Class II
19	13.1527	-0.0295	J181417.83-173231.1	10.529	10.021	7.684	5.341	Class II
20	13.1543	-0.0234	J181416.66-173215.4	10.758	10.158	8.237	6.232	Class II
21	13.1647	-0.0310	J181419.59-173155.6	11.511	10.498	9.022	6.565	Class II
22	13.1577	-0.0263	J181417.72-173209.5	10.568	10.225	8.441	5.908	Class II
23	13.1919	-0.0358	J181423.94-173037.7	10.433	10.010	8.891	6.481	Class II
24	13.1704	-0.0343	J181421.01-173143.2	10.077	9.621	8.265	5.976	Class II
25	13.2038	-0.0395	J181426.20-173006.5	8.941	8.625	7.104	5.237	Class II
26	13.1103	0.0155	J181402.78-173327.7	10.560	10.300	8.813	6.951	Class II
27	13.1370	-0.0034	J181410.17-173235.5	9.904	9.313	8.291	5.669	Class II
28	13.1452	-0.0016	J181410.76-173206.7	10.542	10.097	7.285	4.779	Class II
29	13.1257	-0.0028	J181408.67-173310.3	11.147	10.754	8.995	6.637	Class II
30	13.1362	-0.0003	J181409.38-173232.9	11.275	10.635	8.559	5.484	Class II
31	13.1269	0.0325	J181401.03-173205.8	10.224	9.903	8.315	6.522	Class II
32	13.1505	-0.0153	J181414.43-173213.6	10.636	10.131	8.669	5.761	Class II
33	13.1611	-0.0034	J181413.08-173119.4	10.832	10.136	8.904	5.365	Class II
34	13.1541	0.0016	J181411.12-173133.1	10.988	10.541	8.519	5.942	Class II
35	13.1907	-0.0196	J181420.20-173013.7	10.467	9.685	8.212	7.706	Class II
36	13.1771	-0.0256	J181419.91-173106.9	10.485	10.058	8.892	7.684	Class II
37	13.1959	-0.0330	J181423.81-173020.5	10.700	10.302	8.892	6.814	Class II
38	13.1979	-0.0191	J181420.96-172950.1	11.156	10.463	9.027	6.777	Class II
39	13.1797	-0.0231	J181419.68-173054.4	10.657	10.390	8.281	6.066	Class II
40	13.2025	-0.0207	J181421.88-172938.4	10.453	9.805	8.237	5.412	Class II
41	13.1850	-0.0311	J181422.08-173051.7	11.027	10.458	8.722	6.238	Class II
42	13.1763	-0.0096	J181416.28-173041.9	9.523	8.906	7.872	4.966	Class II
43	13.1529	0.0133	J181408.39-173116.8	11.277	10.554	9.114	5.257	Class II
44	13.1778	0.0060	J181413.01-173010.3	9.489	8.862	7.858	3.911	Class II
45	13.1627	0.0214	J181407.78-173031.9	9.323	8.688	5.991	2.136	Class II
46	13.1732	0.0086	J181411.88-173020.6	10.801	10.366	7.612	3.212	Class II
47	13.1599	0.0238	J181406.92-173036.4	9.450	8.858	6.121	2.438	Class II
48	13.1904	0.0215	J181411.09-172903.8	11.423	10.865	9.270	2.260	Class II
49	13.1951	0.0128	J181413.58-172903.9	9.707	8.801	6.974	2.114	Class II

TABLE 6—*Continued*

Candidate #	l [°]	b [°]	Identification	Fluxes [mag]				Classification
				[3.4]	[4.6]	[12]	[22]	
50	13.2076	0.0148	J181414.64-172821.2	9.698	9.104	6.214	1.898	Class II
51	13.1538	0.0598	J181358.24-172953.7	9.997	9.382	8.095	4.876	Class II
52	13.1348	0.0557	J181356.85-173101.0	9.628	8.946	5.814	2.094	Class II
53	13.1236	0.0950	J181346.80-173028.4	10.652	10.249	8.394	5.963	Class II
54	13.1157	0.0930	J181346.30-173057.0	11.448	11.137	9.105	7.158	Class II
55	13.1554	0.0962	J181350.37-172845.8	10.915	10.286	9.060	8.037	Class II
56	13.2163	0.0706	J181403.36-172617.6	10.970	10.459	7.987	4.483	Class II
57	13.2151	0.0670	J181404.00-172627.5	11.001	10.383	7.583	5.756	Class II
58	13.2071	-0.0271	J181423.84-172934.7	9.319	8.922	7.300	4.959	Class II
59	13.2185	-0.0141	J181422.34-172836.2	10.337	9.983	7.966	4.871	Class II
60	13.2078	-0.0178	J181421.88-172916.6	9.124	8.589	7.523	4.744	Class II
61	13.2179	-0.0213	J181423.85-172850.7	10.761	10.112	7.705	5.931	Class II
62	13.2204	0.0050	J181418.36-172757.4	10.030	9.534	8.327	4.625	Class II
63	13.2143	0.0017	J181418.35-172822.5	10.872	10.285	8.820	4.903	Class II
64	13.2536	-0.0052	J181424.60-172629.9	10.132	9.667	7.969	5.408	Class II
65	13.2532	0.0007	J181423.25-172621.3	11.055	10.557	8.166	5.727	Class II
66	13.2621	0.0030	J181423.79-172549.1	11.615	10.736	9.077	5.965	Class II
67	13.2553	-0.0207	J181428.22-172651.4	9.615	9.146	7.810	5.657	Class II
68	13.2630	-0.0075	J181426.23-172604.1	11.537	10.949	9.479	5.131	Class II
69	13.2440	-0.0054	J181423.50-172700.7	10.056	9.031	7.095	4.135	Class II
70	13.2507	-0.0041	J181424.00-172637.2	10.300	9.913	7.819	5.102	Class II
71	13.2489	0.0039	J181422.01-172629.3	7.988	7.294	5.927	4.050	Class II
72	13.2484	-0.0065	J181424.27-172648.7	10.165	9.770	7.610	5.207	Class II
73	13.2669	-0.0343	J181432.62-172638.0	10.417	9.654	8.019	7.414	Class II
74	13.2583	-0.0373	J181432.25-172710.3	11.407	10.567	8.639	8.173	Class II
75	13.2301	0.0140	J181417.54-172711.3	10.361	9.642	7.410	6.239	Class II
76	13.2255	0.0156	J181416.61-172723.1	9.430	8.754	7.473	4.366	Class II
77	13.2451	0.0341	J181414.88-172549.3	10.995	10.254	7.405	4.293	Class II
78	13.2404	0.0107	J181419.49-172644.6	10.908	9.870	7.559	7.685	Class II
79	13.2343	0.0419	J181411.87-172610.1	9.853	9.426	7.266	4.838	Class II
80	13.2499	0.0332	J181415.66-172535.5	10.933	10.088	7.836	4.427	Class II
81	13.2636	0.0175	J181420.79-172519.2	9.982	9.342	8.087	5.534	Class II
82	13.2574	0.0339	J181416.42-172510.8	11.900	11.196	8.401	5.181	Class II
83	13.2392	0.0430	J181412.20-172552.7	10.673	10.118	8.891	5.524	Class II
84	13.2558	0.0378	J181415.36-172509.1	11.519	11.054	8.415	5.495	Class II
85	13.1292	0.1156	J181342.93-172935.3	10.796	10.527	8.517	6.073	Class II
86	13.1461	0.1132	J181345.50-172845.9	11.101	10.645	8.279	6.229	Class II
87	13.1350	0.1103	J181344.81-172926.0	8.488	7.950	6.759	5.174	Class II
88	13.1616	0.1054	J181349.09-172810.6	11.137	10.402	8.815	5.834	Class II
89	13.1883	0.0892	J181355.88-172714.1	7.892	7.571	6.055	3.938	Class II
90	13.1815	0.1000	J181352.66-172716.9	10.393	9.975	7.960	6.182	Class II
91	13.1945	0.1155	J181350.82-172609.0	10.328	10.050	8.788	6.638	Class II
92	13.1833	0.1066	J181351.44-172659.9	9.333	9.015	7.827	5.732	Class II
93	13.2189	0.0964	J181357.99-172524.8	9.412	8.517	6.523	2.770	Class II
94	13.2282	0.0955	J181359.30-172456.9	10.304	9.777	6.744	3.229	Class II
95	13.2126	0.0974	J181357.00-172543.1	9.804	9.485	7.280	3.962	Class II
96	13.2128	0.1152	J181353.08-172511.7	10.206	9.920	7.349	4.207	Class II
97	13.2164	0.1159	J181353.36-172459.1	9.300	10.050	8.821	4.499	Class II
98	13.2433	0.0710	J181406.52-172451.6	9.465	9.015	6.765	3.092	Class II
99	13.2482	0.0971	J181401.34-172351.1	9.776	9.168	8.050	4.627	Class II

TABLE 6—*Continued*

Candidate #	l [°]	b [°]	Identification	Fluxes [mag]				Classification
				[3.4]	[4.6]	[12]	[22]	
100	13.2679	0.0722	J181409.21-172331.5	11.125	10.261	7.874	4.907	Class II
101	13.2659	0.0771	J181407.89-172329.7	9.496	9.243	7.583	4.824	Class II
102	13.2420	0.1051	J181358.82-172356.7	10.622	10.187	7.297	4.686	Class II
103	13.2390	0.1185	J181355.51-172343.3	10.482	9.921	7.358	4.132	Class II
104	13.1380	-0.0254	J181415.16-173310.3	11.555	11.301	8.303	6.554	Transition Disk
105	13.1131	-0.0255	J181412.18-173429.2	9.828	9.621	8.645	7.095	Transition Disk
106	13.1302	-0.0333	J181415.95-173348.5	9.932	9.692	8.278	6.252	Transition Disk
107	13.1319	-0.0260	J181414.56-173330.7	9.684	9.453	8.130	5.958	Transition Disk
108	13.1630	-0.0390	J181421.17-173214.8	8.383	7.905	7.722	5.794	Transition Disk
109	13.1434	-0.0357	J181418.08-173311.0	10.852	10.078	9.131	7.067	Transition Disk
110	13.1559	-0.0304	J181418.41-173222.5	8.913	8.355	7.577	5.329	Transition Disk
111	13.1591	-0.0291	J181418.52-173210.1	8.583	8.237	8.206	6.513	Transition Disk
112	13.1685	-0.0357	J181421.10-173151.7	9.228	8.592	8.107	6.014	Transition Disk
113	13.1178	-0.0041	J181408.01-173337.4	10.642	9.930	9.228	6.738	Transition Disk
114	13.1414	-0.0040	J181410.84-173222.7	11.260	10.857	7.784	5.008	Transition Disk
115	13.1429	-0.0156	J181413.57-173237.9	8.265	8.045	8.394	6.546	Transition Disk
116	13.1471	0.0039	J181409.76-173151.2	10.965	10.559	7.662	5.014	Transition Disk
117	13.1338	0.0047	J181408.00-173231.7	11.836	11.295	8.002	5.328	Transition Disk
118	13.1148	0.0518	J181355.31-173210.8	11.336	11.114	7.206	5.035	Transition Disk
119	13.1511	0.0367	J181403.02-173042.0	10.622	10.453	9.851	5.419	Transition Disk
120	13.1361	0.0203	J181404.83-173157.6	7.942	7.328	6.682	4.696	Transition Disk
121	13.1737	-0.0160	J181417.38-173101.2	11.805	11.355	8.017	4.768	Transition Disk
122	13.1491	-0.0062	J181412.24-173202.1	9.232	9.026	7.356	4.807	Transition Disk
123	13.1801	-0.0195	J181418.90-173047.1	9.321	8.778	7.815	5.611	Transition Disk
124	13.1889	-0.0263	J181421.47-173031.1	11.226	10.936	7.854	6.182	Transition Disk
125	13.1775	-0.0162	J181417.88-173049.7	10.607	10.353	7.602	4.404	Transition Disk
126	13.1810	-0.0299	J181421.31-173102.2	12.121	11.943	8.638	5.979	Transition Disk
127	13.1864	-0.0094	J181417.43-173009.7	10.567	10.264	9.263	6.273	Transition Disk
128	13.1724	0.0203	J181409.19-173002.7	11.192	10.765	5.473	1.320	Transition Disk
129	13.1668	0.0212	J181408.31-173019.1	10.302	9.588	5.375	0.938	Transition Disk
130	13.1777	0.0131	J181411.42-172958.4	10.984	10.516	9.688	3.001	Transition Disk
131	13.1698	0.0259	J181407.64-173001.4	9.631	9.229	5.086	0.549	Transition Disk
132	13.1665	0.0306	J181406.20-173003.7	10.611	9.836	4.188	-0.772	Transition Disk
133	13.1861	0.0172	J181411.53-172925.0	7.226	6.464	5.898	1.992	Transition Disk
134	13.2099	0.0177	J181414.29-172808.9	11.603	10.824	5.747	1.936	Transition Disk
135	13.1981	0.0108	J181414.38-172858.1	11.703	11.179	6.253	1.919	Transition Disk
136	13.2055	0.0025	J181417.10-172849.0	11.824	11.332	7.058	3.638	Transition Disk
137	13.2126	0.0194	J181414.22-172757.5	12.147	11.623	6.538	1.997	Transition Disk
138	13.1858	0.0049	J181414.20-172947.0	10.778	10.507	7.445	4.071	Transition Disk
139	13.1303	0.0691	J181353.35-173052.1	9.467	9.299	7.496	4.097	Transition Disk
140	13.1286	0.0610	J181354.93-173111.4	10.033	9.571	4.676	2.042	Transition Disk
141	13.1316	0.0521	J181357.26-173117.1	10.701	10.087	6.685	3.236	Transition Disk
142	13.1122	0.0773	J181349.34-173135.1	10.111	9.883	10.262	7.892	Transition Disk
143	13.1187	0.0564	J181354.75-173150.5	11.499	11.298	6.807	4.052	Transition Disk
144	13.1589	0.0387	J181403.50-173014.0	9.631	8.931	5.122	0.934	Transition Disk
145	13.1421	0.0526	J181358.42-173043.0	11.134	10.699	6.780	3.402	Transition Disk
146	13.1280	0.0967	J181346.96-173011.5	9.944	9.647	8.528	6.409	Transition Disk
147	13.1250	0.0795	J181350.40-173050.9	8.393	8.130	7.594	5.493	Transition Disk
148	13.1524	0.0761	J181354.44-172930.1	8.655	8.281	7.398	5.147	Transition Disk

TABLE 6—*Continued*

Candidate #	l [°]	b [°]	Identification	Fluxes [mag]				Classification
				[3.4]	[4.6]	[12]	[22]	
149	13.1753	0.0488	J181403.24-172904.5	9.535	8.937	2.135	-2.611	Transition Disk
150	13.1832	0.0570	J181402.39-172825.6	10.112	9.869	3.703	-0.608	Transition Disk
151	13.1712	0.0418	J181404.30-172929.5	10.602	10.088	3.017	-1.599	Transition Disk
152	13.1826	0.0528	J181403.24-172834.6	9.907	9.260	1.655	-2.432	Transition Disk
153	13.1639	0.0376	J181404.35-173000.0	10.127	9.568	3.913	-0.276	Transition Disk
154	13.1713	0.0395	J181404.81-172933.3	11.091	10.374	3.963	-0.653	Transition Disk
155	13.2105	0.0229	J181413.21-172758.0	11.888	11.416	5.427	1.524	Transition Disk
156	13.2038	0.0461	J181407.28-172739.2	10.341	9.920	4.262	-0.182	Transition Disk
157	13.2089	0.0266	J181412.20-172756.8	11.358	10.652	5.704	0.822	Transition Disk
158	13.2130	0.0355	J181410.72-172728.4	10.631	10.347	4.588	1.039	Transition Disk
159	13.2103	0.0242	J181412.89-172756.1	11.682	10.981	5.123	1.075	Transition Disk
160	13.1939	0.0384	J181407.78-172823.8	10.681	9.957	2.256	-2.989	Transition Disk
161	13.1896	0.0791	J181358.26-172727.3	10.666	10.425	6.035	3.807	Transition Disk
162	13.1801	0.0761	J181357.79-172802.5	9.975	9.662	6.309	3.485	Transition Disk
163	13.1976	0.0803	J181358.98-172659.8	11.393	10.948	7.773	3.752	Transition Disk
164	13.1915	0.0868	J181356.80-172708.0	11.358	10.833	6.953	4.164	Transition Disk
165	13.1984	0.0722	J181400.85-172711.2	11.740	11.317	6.627	3.467	Transition Disk
166	13.1974	0.0662	J181402.06-172724.8	10.170	9.973	5.734	1.855	Transition Disk
167	13.2222	0.0750	J181403.09-172551.2	9.327	8.771	8.291	2.102	Transition Disk
168	13.2081	0.0561	J181405.57-172708.5	10.739	10.058	4.434	0.552	Transition Disk
169	13.2017	-0.0300	J181423.83-172956.8	11.641	11.337	7.013	4.566	Transition Disk
170	13.2052	-0.0235	J181422.82-172934.6	11.378	11.212	7.666	5.331	Transition Disk
171	13.2266	-0.0156	J181423.66-172813.2	11.528	11.375	8.565	5.659	Transition Disk
172	13.2147	-0.0087	J181420.69-172839.2	11.950	11.775	8.072	5.042	Transition Disk
173	13.2250	0.0111	J181417.54-172732.5	10.599	10.406	8.002	5.212	Transition Disk
174	13.2556	-0.0021	J181424.15-172618.2	10.899	10.461	9.358	5.608	Transition Disk
175	13.2439	0.0016	J181421.94-172648.9	10.058	9.892	6.862	4.494	Transition Disk
176	13.2406	0.0040	J181421.00-172655.2	11.241	11.043	6.649	4.894	Transition Disk
177	13.2484	0.0094	J181420.74-172621.2	11.502	11.349	7.695	5.089	Transition Disk
178	13.2676	0.0133	J181422.20-172514.1	9.564	9.109	8.739	6.273	Transition Disk
179	13.2318	0.0604	J181407.47-172546.1	9.299	9.099	7.004	4.299	Transition Disk
180	13.2297	0.0737	J181404.30-172529.9	9.594	9.317	4.814	1.510	Transition Disk
181	13.2416	0.0659	J181407.44-172505.7	10.003	9.658	6.606	3.980	Transition Disk
182	13.2338	0.0719	J181405.18-172519.8	12.536	11.969	5.976	1.548	Transition Disk
183	13.2315	0.0551	J181408.63-172556.0	10.239	10.048	7.724	5.911	Transition Disk
184	13.2344	0.0724	J181405.15-172517.3	12.369	11.834	5.563	1.525	Transition Disk
185	13.2363	0.0654	J181406.92-172523.1	10.862	10.665	6.555	3.011	Transition Disk
186	13.1462	0.1193	J181344.17-172835.2	9.092	8.479	7.845	5.891	Transition Disk
187	13.1188	0.1113	J181342.64-173015.7	10.204	9.787	8.924	6.601	Transition Disk
188	13.1502	0.1042	J181347.97-172848.4	9.896	9.186	8.720	6.425	Transition Disk
189	13.1501	0.1144	J181345.71-172831.4	9.305	9.117	8.257	6.510	Transition Disk
190	13.1924	0.0975	J181354.55-172646.7	9.473	9.250	8.793	4.548	Transition Disk
191	13.1979	0.1120	J181352.00-172604.4	8.698	8.412	8.768	6.937	Transition Disk
192	13.1957	0.0886	J181356.90-172651.6	11.635	11.142	6.151	3.423	Transition Disk
193	13.2292	0.0910	J181400.42-172501.5	11.600	11.348	6.060	1.161	Transition Disk
194	13.2239	0.0903	J181359.92-172519.4	12.463	11.933	7.178	1.502	Transition Disk
195	13.2226	0.1037	J181356.81-172500.8	11.410	10.976	6.355	3.515	Transition Disk
196	13.2203	0.1024	J181356.83-172510.0	10.970	10.501	5.847	3.271	Transition Disk
197	13.2295	0.0835	J181402.10-172513.4	11.661	11.143	5.267	0.385	Transition Disk
198	13.2246	0.1026	J181357.29-172456.0	10.644	10.153	5.588	3.409	Transition Disk

TABLE 6—*Continued*

Candidate #	l [°]	b [°]	Identification	Fluxes [mag]				Classification
				[3.4]	[4.6]	[12]	[22]	
199	13.2298	0.0885	J181401.03-172504.1	11.742	11.114	5.584	1.075	Transition Disk
200	13.2252	0.0813	J181402.07-172530.9	10.578	10.153	6.911	0.759	Transition Disk
201	13.2284	0.1016	J181357.97-172445.8	12.267	11.619	5.539	3.212	Transition Disk
202	13.2280	0.0838	J181401.85-172517.7	11.410	11.135	5.899	0.356	Transition Disk
203	13.2127	0.0831	J181400.16-172607.3	8.735	8.405	7.955	4.510	Transition Disk
204	13.2229	0.0911	J181359.62-172521.4	11.294	10.889	7.497	2.031	Transition Disk
205	13.2372	0.1141	J181356.27-172356.5	8.749	8.517	7.132	4.033	Transition Disk
206	13.2136	0.1166	J181352.87-172507.0	11.056	10.724	7.227	4.170	Transition Disk
207	13.2205	0.1102	J181355.12-172455.8	10.310	10.150	7.548	4.420	Transition Disk
208	13.2377	0.0983	J181359.81-172422.0	12.059	11.550	6.093	3.520	Transition Disk
209	13.2404	0.0764	J181404.99-172451.4	9.730	9.387	4.296	1.688	Transition Disk
210	13.2385	0.0818	J181403.55-172448.1	10.547	9.932	4.625	1.282	Transition Disk
211	13.2315	0.0864	J181401.70-172502.2	12.504	12.291	5.677	0.618	Transition Disk
212	13.2323	0.0929	J181400.37-172448.5	11.057	10.655	6.449	2.195	Transition Disk
213	13.2312	0.0824	J181402.55-172510.2	10.613	9.946	4.475	-0.268	Transition Disk
214	13.2292	0.0787	J181403.12-172522.9	9.237	9.014	3.736	0.416	Transition Disk
215	13.2371	0.0936	J181400.78-172432.1	10.320	9.876	5.402	2.454	Transition Disk
216	13.2325	0.0770	J181403.89-172515.4	10.064	9.692	5.063	-0.432	Transition Disk
217	13.2404	0.0940	J181401.08-172421.0	9.943	9.723	4.805	3.131	Transition Disk
218	13.2435	0.0771	J181405.21-172440.2	11.152	10.697	6.127	2.319	Transition Disk
219	13.2468	0.0740	J181406.27-172435.2	11.786	11.424	7.352	4.218	Transition Disk
220	13.2352	0.0992	J181359.33-172428.5	9.378	9.056	5.712	2.634	Transition Disk
221	13.2516	0.0858	J181404.24-172359.7	8.614	8.314	7.176	4.687	Transition Disk
222	13.2427	0.0814	J181404.14-172435.4	10.319	10.027	4.899	2.521	Transition Disk
223	13.2390	0.0928	J181401.19-172427.4	9.106	8.818	5.859	2.362	Transition Disk
224	13.2471	0.0781	J181405.40-172427.1	10.256	10.098	6.963	3.952	Transition Disk
225	13.2354	0.0725	J181405.22-172513.9	10.123	9.731	4.448	1.682	Transition Disk
226	13.2422	0.0887	J181402.49-172424.4	10.677	10.362	5.643	2.381	Transition Disk
227	13.2676	0.0821	J181407.00-172315.7	10.238	10.018	7.799	5.071	Transition Disk
228	13.2696	0.0742	J181408.98-172322.8	10.599	10.386	7.460	4.081	Transition Disk
229	13.2668	0.0850	J181406.25-172313.1	10.240	9.574	8.588	5.451	Transition Disk
230	13.2589	0.0796	J181406.49-172347.4	7.302	6.825	6.675	4.609	Transition Disk
231	13.2457	0.1019	J181400.00-172350.7	9.816	9.327	10.194	5.108	Transition Disk
232	13.2399	0.1093	J181357.66-172356.3	9.114	8.881	7.718	4.412	Transition Disk
233	13.2487	0.1005	J181400.65-172343.4	10.996	10.360	11.104	6.363	Transition Disk
234	13.2372	0.1034	J181358.63-172415.1	9.272	8.958	6.258	3.162	Transition Disk

NOTE.—Table 6 is published in its entirety in the electronic edition of the *Astrophysical Journal*. A portion is shown here for guidance regarding its form and content.



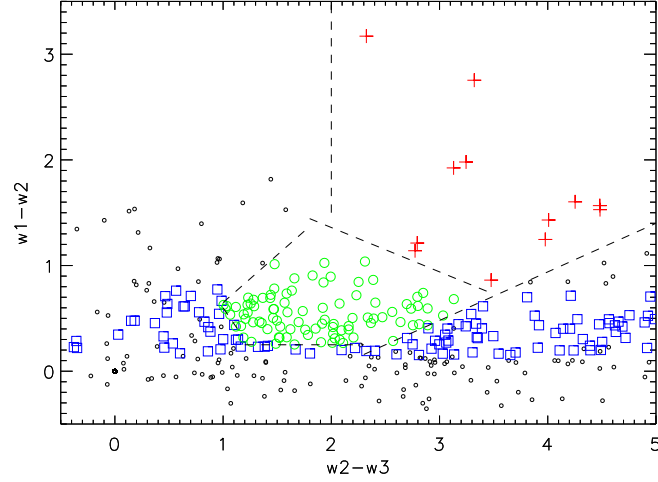


Fig. 12.— Color-color diagram  $w1-w2$  versus  $w2-w3$  of the candidate YSOs around N10. Red crosses: Class I objects; green circles: Class II objects, blue squares: transition disk objects. The dashed lines indicate the limits of the regions according to HL. The transition disks were not defined by means of this diagram. The remaining objects are indicated by black dots.

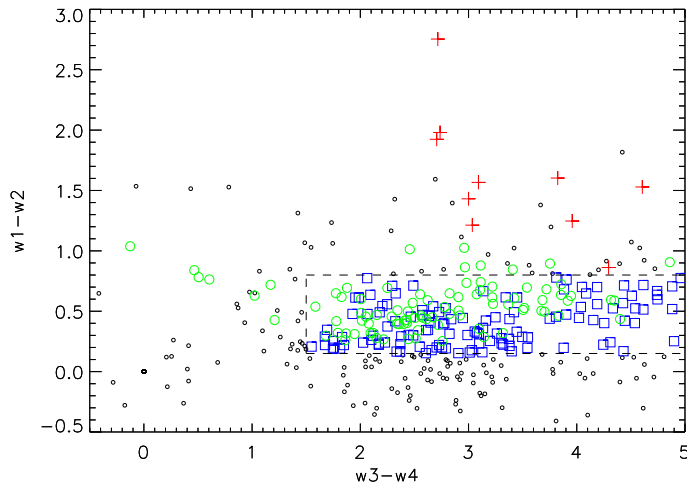


Fig. 13.— Color-color diagram  $w1-w2$  versus  $w3-w4$ , like Figure 12. The box used to define transition-disk objects (in blue) also contains many Class II objects (green circles) because these objects were defined to be Class II in a previous step using another color-color diagram (Figure 12).

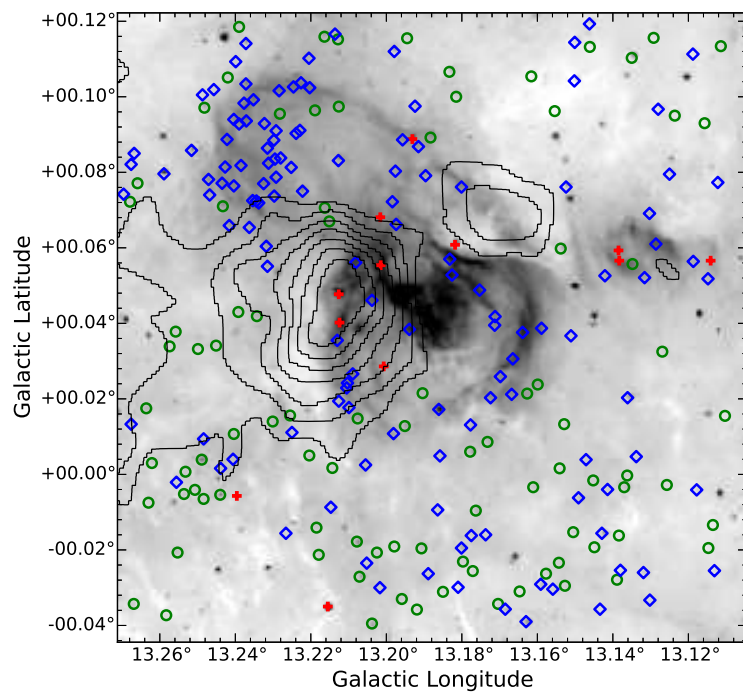


Fig. 14.— Distribution of the identified YSOs. Background is Spitzer 8.0  $\mu\text{m}$  image. Red crosses are Class I sources; green circles are class II sources; blue diamonds are "transition disk" sources. Black contours shows the  $^{13}\text{CO}$  emission around the bubble.

## 5. Discussion

In this section we discuss the distribution of molecular material around the bubble N10 and its connection with the star formation history.

### 5.1. Surrounding gas of N10

Channel maps are presented in Figure 5; since  $^{12}\text{CO}$  is optically thick, it appears to be spread over a large area, whereas  $^{13}\text{CO}$  traces the denser regions, once it is optically thinner. Figure 10 displays two peaks of molecular emission, i.e. two  $^{13}\text{CO}$  condensations. Clump #1 is centered at  $l = 13.218^\circ$ ,  $b = 0.043^\circ$  and Clump #2 is located at  $l = 13.169^\circ$ ,  $b = 0.072^\circ$ . The two clumps are located precisely on the edge of the ring structure revealed by the  $8.0\ \mu\text{m}$  emission and highlighted by an ellipse in Figure 2.

In order to verify the dynamical status of the clumps, we compare the gas mass in LTE and the virial mass calculated in Subsection 4.4 for each clump. The two clumps have greater  $M_{\text{virial}}$  than  $M_{\text{LTE}}$ , implying that they are gravitationally unbound, indicating currently there is no star in forming (e.g. Yuan et al. 2014; Liu et al. 2016).

### 5.2. Other components of CO emission

As highlighted in subsection 4.1 CO components at 20 and  $37\ \text{km s}^{-1}$  do not seem to be physically related with bubble N10. Which could be the origin of this contribution? It is known CO emission in galaxies is concentrated in spiral arms (Nieten et al. 2006; Schinnerer et al. 2013). The line of sight towards N10 crosses two spiral arms before reaching the distance 4.7 kpc (see e.g. Figure 10 of Hou & Han 2014). The velocities of peaks 20 and  $37\ \text{km s}^{-1}$  correspond to near kinematic distances of 2.4 and 3.7 kpc respectively, representing roughly to the distance of those arms.

It is therefore reasonable to suppose these two velocity peaks are associated with foreground gas situated in distinct spiral arms. Furthermore, emission at these two velocities does not seem to be correlated with geometry of N10; emission appears to be irregularly spread over studied field. If one examines the Figure 4 of the  $^{13}\text{CO}$  (1–0) survey of the Galaxy by Lee et al. (2001), selecting the panel corresponding to  $b = 0.05^\circ$ , one can see at longitude  $13.2^\circ$  the presence of  $^{13}\text{CO}$  at about 50, 35 and  $20\ \text{km s}^{-1}$ . The last two ones are part of elongated structures in the longitude-

velocity diagram (extending to higher and lower longitudes) that are usually interpreted as spiral arms. In this region of the diagram, lower velocities correspond to closest arms.

Note that kinematic distances are uncertain at longitudes close to the Galactic center. We have to make use of a  $^{13}\text{CO}$  survey because in  $^{12}\text{CO}$  longitude-velocity diagrams, the spiral arms are wider in velocity, and are not seen separated.

### 5.3. Situation of star formation

The densest clump in the  $870\ \mu\text{m}$  emission seems to be a candidate region to form stellar clusters, since it have a total mass of  $M_{\text{tot}} = 240\ M_\odot$  and a mean radius of  $R = 0.36\ \text{pc}$ . In accordance with Motte et al. (2003) fragments in the range between 0.09 and 0.56 pc and masses covering a range from 20 to  $3600\ M_\odot$  have characteristics of protoclusters.

Elmegreen & Lada (1977) was the first to propose the scenario of “Collect and Collapse” where the radiation of the massive stars of an HII region creates an ionization front at the interface with the molecular cloud, that drives the propagation of a shock front into the neutral material and which accumulates mass and eventually becomes gravitationally unstable. Other scenarios of triggered star formation have been proposed, like e.g. the “Radiation-Driven Implosion” model, based on the over pressure exerted by the ionized gas, suggested by Lefloch & Lazareff (1994). While “Collect and Collapse” model takes place in a large spatial size ( $\sim 10\ \text{pc}$ ) with a longer timescale (a few Myr), “Radiation-Driven Implosion” takes place in  $\sim 1\ \text{pc}$  with a timescale of 0.5 Myr.

Although we found evidences for active star formation in N10, we are not sure that the formation of these YSOs were triggered by the “Collect and Collapse” mechanism around the infrared bubble. In order to verify if this process is viable we can apply the analytical model proposed by Whitworth et al. (1994) and compare the fragmentation time scale  $t_{\text{frag}}$  with the dynamical age  $t_{\text{dyn}}$  of the region. The Whitworth et al. (1994) model describes the fragmentation time as:

$$t_{\text{frag}} = 1.56\ c_s^{7/11}\ N_{\text{uv}}^{-1/11}\ n_o^{-5/11}, \quad (15)$$

where  $c_s$  is the isothermal sound speed in the ionized gas in the shocked layer in units of  $0.2\ \text{km s}^{-1}$ ,  $N_{\text{uv}}$  is the ionizing photon flux in units of  $10^{49}\ \text{photons.s}^{-1}$

and  $n_o$  is the initial particle number density of the ambient neutral gas in units of  $10^3 \text{ cm}^{-3}$ . Considering  $c_s = 0.2 \text{ km s}^{-1}$  (Liu et al. 2012),  $N_{uv} = 1.86 \times 10^{49} \text{ photons.s}^{-1}$  and  $n_o \sim 10^3 \text{ cm}^{-3}$  (Ma et al. 2013) we estimated  $t_{frag} \sim 1.5 \times 10^6 \text{ yr}$  for the region. From Ma et al. (2013)  $t_{dyn} = 9.17 \times 10^4 \text{ yr}$ , i.e. the dynamical age is smaller than the fragmentation time scale, which indicates that the region do not support the “Collect and Collapse” mechanism. In this case the “Radiation-Driven Implosion” could be considered and further investigated.

The position of YSOs compared with CO distribution indicates that stars are forming inside the molecular clumps. Figure 14 shows the spatial distribution of identified YSOs from the Table 6. In fact the Class I YSOs candidates to be associated to N10 presented in Table 5 have ages smaller than the fragmentation time scale, suggesting a possibility of triggered star formation by pre-existing condensations compressed by the pressure of the ionized gas, as “Radiation-Driven Implosion” scenario proposes.

#### 5.4. The bubble N11

Infrared images shows N11, a bubble that seems to be physically connected to N10 and extends about 3 pc in the up-right direction. Conversely the molecular distribution of N11 does not suggest a physical connection with N10, since the emission of  $^{13}\text{CO}$  ( $J = 1 - 0$ ) between 47 and  $53 \text{ km s}^{-1}$  is not coincident with  $8.0 \mu\text{m}$  emission.

It is probable that this object is a remnant of an HII region, where the lack of 20 cm emission lead us to consider there is no more ionized gas inside. It is likely that other energy source has triggered the formation of these YSOs, such as the explosion of a type II supernova.

Class I YSOs do not seem to be superimposed on the bubble N11 and many Class II YSOs can be found towards N11, as we can see in the Figure 14. There is a remarkable concentration of transition disk sources surrounding the top frontier of N11. We consider, in this interpretation, that the concentration of Class II YSOs near the upper frontier of N11 is possibly the result of a past star formation activity related to that bubble.

#### 5.5. A small bubble to the right of N10: MWP1G013134+000580

The bubble MWP1G013134+000580, at coordinates  $l = 13.134^\circ$  and  $b = 0.058^\circ$ , has size smaller than 2 pc. Interestingly this small bubble should have the about the same distance of N10, since its CO emission is contained in the same main velocity peak, clearly seen in channel maps with velocities between 51 and  $53 \text{ km s}^{-1}$  in Figure 5.

We found three Class I YSOs in the region covered by  $8.0 \mu\text{m}$  emission of MWP1G013134+000580. The age of the small bubble seems to have the same order of N10, as we can infer from the evolutionary stages of the YSOs.

### 6. Conclusions

We have performed a comprehensive study of the infrared bubble N10 using the molecular line emissions of  $^{12}\text{CO}$  ( $J = 1 - 0$ ) and  $^{13}\text{CO}$  ( $J = 1 - 0$ ), mid-infrared Spitzer-GLIMPSE and MIPS GAL images, VLA data of the 20 cm emission, APEX observations of the continuum  $870 \mu\text{m}$  emission and WISE catalog of mid-infrared point sources. The key results are summarized as follows:

1. We observed the  $J = 1 - 0$  transition of CO isotopologues at PMO 13.7-m radio telescope. The distribution of the CO emission showed that the molecular gas around the bubble N10 has velocity  $V_{lsr} = 52.6 \text{ km s}^{-1}$ , from which we estimated distance  $D = 4.7 \pm 0.5 \text{ kpc}$ . This observations revealed two  $^{13}\text{CO}$  clumps with  $M_{LTE} \sim 2 \times 10^3 M_\odot$ ,  $M_{virial} \sim 8.5 \times 10^3 M_\odot$  and  $M_{Jeans} \sim 6 \times 10^3 M_\odot$ , which means that the clumps implying that they are gravitationally unbound currently.
2. The emission of radio continuum and the presence of  $24 \mu\text{m}$  emission suggest ionizing sources inside the bubble. We estimated a total flux of 20 cm of  $F_{20 \text{ cm}} = 1.17 \text{ Jy}$  and an electron density of  $n_e \sim 130 \text{ cm}^{-3}$ , with a Lyman continuum photon flux of  $N_{uv} = 1.86 \times 10^{49} \text{ ionizing photons s}^{-1}$ , equivalent to an  $\sim \text{O7 V}$  star (or stars) keeping the gas ionized.
3. Two cold dust clumps were identified towards N10 in LABOCA/APEX images. For the densest clump, we estimated from emission at  $870 \mu\text{m}$  a total mass of  $M_{tot} = 240 M_\odot$ , a mean radius of  $R_D = 0.36 \text{ pc}$ , a column density of

$N(H_2) = 6.3 \times 10^{22} \text{ cm}^{-2}$  and an average volume density of  $n(H_2) = 9.4 \times 10^4 \text{ cm}^{-3}$ , physical characteristics indicating that this condensation is a good candidate of protocluster.

4. We identified 234 YSOs in the whole region: 12 of them classified as Class I, 91 Class II and 131 Transition Disks. We fitted the SED for Class I YSOs candidates identified from #1 to #9 and we derived their physical parameters. From the models we found stellar ages ranging from  $\sim 10^3$  to  $10^6$  yr. By comparing the estimated dynamical age ( $t_{\text{dyn}} = 9.17 \times 10^4$  yr) and the fragmentation time scale ( $t_{\text{frag}} \sim 1.5 \times 10^6$  yr) we infer that star formation can be triggered as a consequence of the “Radiation-Driven Implosion” process. Likewise, the age range for the Class I YSOs are below that found for the fragmentation time scale, indicating they were formed before the collect molecular cloud became gravitationally unstable to fragment to form stars.
5. In the Spitzer 8.0  $\mu\text{m}$  image the infrared bubble N11 can be seen in the direction of the N10, however one is not physically connected with other. Class II YSOs appears towards N11, suggesting that this could be a remnant of HII region. A third infrared bubble, the small MWPIG013134+000580, appears in the observed field and, interestingly, has CO emission in the same main velocity as N10 and seems to shelter some evolved YSOs.

We gratefully acknowledge the contribution of Tie Liu, who provided some of the scripts used in this work. We also give our thanks Cristina Cappa and Bertrand Lefloch for the helpful discussion. We thank the anonymous referee for useful comments and suggestions that led to a improved version of the original article. This work is supported by the National Natural Science Foundation of China through grant NSFC 11373009-11433008. J.Y is supported by the National Natural Science Foundation of China through grants of 11503035 and 11573036. EM acknowledges support from the Brazilian agency FAPESP under the grants 2014/22095-6 and 2015/22254-0. We are grateful to the staffs at the Qinghai Station of PMO for their hospitality and assistance during the observations. We thank the Key Laboratory for Radio Astronomy, CAS, for partial support in the operation of the telescope.

## REFERENCES

- Amôres, E. B., & Lépine, J. R. D. 2005, *AJ*, 130, 659
- Anderson, L. D., Bania, T. M., Balser, D. S., et al. 2014, *ApJS*, 212, 1
- Beaumont, C. N., & Williams, J. P. 2010, *ApJ*, 709, 791
- Becker, R. H., White, R. L., Helfand, D. J., & Zoone-matkermani, S. 1994, *ApJS*, 91, 347
- Benjamin, R. A., Churchwell, E., Babler, B. L., et al. 2003, *PASP*, 115, 953
- Bergin, E. A., & Tafalla, M. 2007, *ARA&A*, 45, 339
- Beuther, H., Linz, H., Henning, T., et al. 2011, *A&A*, 531, AA26
- Blaauw, A. 1991, *NATO ASIC Proc. 342: The Physics of Star Formation and Early Stellar Evolution*, 125
- Brand, J., & Blitz, L. 1993, *A&A*, 275, 67
- Bressert, E., Bastian, N., Gutermuth, R., et al. 2010, *MNRAS*, 409, L54
- Cappa, C. E., Rubio, M., Martín, M. C., & Romero, G. A. 2009, *A&A*, 508, 759
- Cappa, C. E., Duronea, N., Firpo, V., et al. 2016, *A&A*, 585, A30
- Churchwell, E., Povich, M. S., Allen, D., et al. 2006, *ApJ*, 649, 759
- Churchwell, E., Watson, D. F., Povich, M. S., et al. 2007, *ApJ*, 670, 428
- Churchwell, E., Babler, B. L., Meade, M. R., et al. 2009, *PASP*, 121, 213
- Condon, J. J., Cotton, W. D., Greisen, E. W., et al. 1998, *AJ*, 115, 1693
- Cutri, R. M., & IPAC/WISE Science Data Center Team 2011, *Bulletin of the American Astronomical Society*, 43, #301.02
- Cutri, R. M., et al. 2013, *VizieR Online Data Catalog*, 2328, 0
- Dale, J. E., Bonnell, I. A., Clarke, C. J., & Bate, M. R. 2005, *MNRAS*, 358, 291
- Dale, J. E., & Bonnell, I. A. 2008, *MNRAS*, 391, 2



- Deharveng, L., Lefloch, B., Kurtz, S., et al. 2008, A&A, 482, 585
- Deharveng, L., Schuller, F., Anderson, L. D., et al. 2010, A&A, 523, A6
- Dewangan, L. K., Ojha, D. K., Anandarao, B. G., Ghosh, S. K., & Chakraborti, S. 2012, ApJ, 756, 151
- Deharveng, L., Zavagno, A., Samal, M. R., et al. 2015, A&A, 582, A1
- Dewangan, L. K., & Ojha, D. K. 2013, MNRAS, 429, 1386
- Dewangan, L. K., Ojha, D. K., Grave, J. M. C., & Mallick, K. K. 2015, MNRAS, 446, 2640
- Draine, B. T., & Anderson, N. 1985, ApJ, 292, 494
- Duronea, N. U., Vasquez, J., Gómez, L., et al. 2015, A&A, 582, A2
- Dyson, J. E., & Williams, D. A. 1980, New York, Halsted Press, 1980. 204 p.,
- Elmegreen, B. G., & Lada, C. J. 1977, ApJ, 214, 725
- Fazio, G. G., Hora, J. L., Allen, L. E., et al. 2004, ApJS, 154, 10
- Feigelson, E. D., & Montmerle, T. 1999, ARA&A, 37, 363
- Garden, R. P., Hayashi, M., Hasegawa, T., Gatley, I., & Kaifu, N. 1991, ApJ, 374, 540
- Gutermuth, R. A., Megeath, S. T., Myers, P. C., et al. 2009, ApJS, 184, 18
- Helfand, D. J., Becker, R. H., White, R. L., Fallon, A., & Tuttle, S. 2006, AJ, 131, 2525
- Hildebrand, R. H. 1983, QJRAS, 24, 267
- Hou, L. G., & Han, J. L. 2014, A&A, 569, AA125
- Huang, S.-S. 1954, AJ, 59, 137
- Ji, W.-G., Zhou, J.-J., Esimbek, J., et al. 2012, A&A, 544, A39
- Kendrew, S., Simpson, R., Bressert, E., et al. 2012, ApJ, 755, 71
- Kendrew, S., Zieleniewski, S., Houghton, R. C. W., et al. 2016, MNRAS, 458, 2405
- Koenig, X. P., Leisawitz, D. T., Benford, D. J., et al. 2012, ApJ, 744, 130
- Koenig, X. P., & Leisawitz, D. T. 2014, ApJ, 791, 131
- Lee, J.-K., Walsh, A. J., Burton, M. G., & Ashley, M. C. B. 2001, MNRAS, 324, 1102
- Lefloch, B., & Lazareff, B. 1994, A&A, 289, 559
- Lefloch, B., Cernicharo, J., Rodríguez, L. F., et al. 2002, ApJ, 581, 335
- Lefloch, B., Cernicharo, J., Cabrit, S., & Cesarsky, D. 2005, A&A, 433, 217
- Liu, T., Wu, Y., Zhang, H., & Qin, S.-L. 2012, ApJ, 751, 68
- Liu, H.-L., Wu, Y., Li, J., et al. 2015, ApJ, 798, 30
- Liu, H.-L., Li, J.-Z., Wu, Y., et al. 2016, ApJ, 818, 95
- Lockman, F. J. 1989, ApJS, 71, 469
- Ma, Y., Zhou, J., Esimbek, J., et al. 2013, Ap&SS, 345, 297
- Mathis, J. S., Rumpl, W., & Nordsieck, K. H. 1977, ApJ, 217, 425
- Matsakis, D. N., Evans, N. J., II, Sato, T., & Zuckerman, B. 1976, AJ, 81, 172
- Minier, V., & Booth, R. S. 2002, A&A, 387, 179
- Miettinen, O. 2012, A&A, 542, A101
- Motte, F., Schilke, P., & Lis, D. C. 2003, ApJ, 582, 277
- Nieten, C., Neininger, N., Guélin, M., et al. 2006, A&A, 453, 459
- Panagia, N., & Walmsley, C. M. 1978, A&A, 70, 411
- Pandian, J. D., & Goldsmith, P. F. 2007, ApJ, 669, 435
- Pandian, J. D., Momjian, E., & Goldsmith, P. F. 2008, A&A, 486, 191
- Paladini, R., Umana, G., Veneziani, M., et al. 2012, ApJ, 760, 149
- Pillai, T., Wyrowski, F., Hatchell, J., Gibb, A. G., & Thompson, M. A. 2007, A&A, 467, 207
- Reich, W., Fuerst, E., Reich, P., & Reif, K. 1990, A&AS, 85, 633

- Rieke, G. H., Young, E. T., Engelbracht, C. W., et al. 2004, *ApJS*, 154, 25
- Robitaille, T. P., Whitney, B. A., Indebetouw, R., & Wood, K. 2007, *ApJS*, 169, 328
- Roman-Duval, J., Jackson, J. M., Heyer, M., et al. 2009, *ApJ*, 699, 1153
- Samal, M. R., Zavagno, A., Deharveng, L., et al. 2014, *A&A*, 566, A122
- Sault, R. J., Teuben, P. J., & Wright, M. C. H. 1995, *Astronomical Data Analysis Software and Systems IV*, 77, 433
- Schinnerer, E., Meidt, S. E., Pety, J., et al. 2013, *ApJ*, 779, 42
- Schuller, F., Menten, K. M., Contreras, Y., et al. 2009, *A&A*, 504, 415
- Shan, W., Yang, J., Shi, S., et al. 2012, *Transactions on Terahertz Science and Technology*, 2, 593
- Simpson, R. J., Povich, M. S., Kendrew, S., et al. 2012, *MNRAS*, 424, 2442
- Stahler, S. W., & Palla, F. 2005, *The Formation of Stars*, by Steven W. Stahler, Francesco Palla, pp. 865. ISBN 3-527-40559-3. Wiley-VCH, January 2005
- Szymczak, M., Hrynek, G., & Kus, A. J. 2000, *A&AS*, 143, 269
- Szymczak, M., Kus, A. J., Hrynek, G., Kępa, A., & Pazderski, E. 2002, *A&A*, 392, 277
- Tackenberg, J., Beuther, H., Henning, T., et al. 2012, *A&A*, 540, AA113
- Thompson, M. A., Hatchell, J., Walsh, A. J., MacDonald, G. H., & Millar, T. J. 2006, *A&A*, 453, 1003
- Thompson, M. A., Urquhart, J. S., Moore, T. J. T., & Morgan, L. K. 2012, *MNRAS*, 421, 408
- Ungerechts, H., Umbanhowar, P., & Thaddeus, P. 2000, *ApJ*, 537, 221
- Watson, C., Povich, M. S., Churchwell, E. B., et al. 2008, *ApJ*, 681, 1341
- Whitworth, A. P., Bhattal, A. S., Chapman, S. J., Disney, M. J., & Turner, J. A. 1994, *MNRAS*, 268, 291
- Wienen, M., Wyrowski, F., Schuller, F., et al. 2012, *A&A*, 544, A146
- Wilson, T. L., & Rood, R. 1994, *ARA&A*, 32, 191
- Wright, E. L., Eisenhardt, P. R. M., Mainzer, A. K., et al. 2010, *AJ*, 140, 1868
- Wu, Y., Liu, T., Meng, F., et al. 2012, *ApJ*, 756, 76
- Yuan, J.-H., Wu, Y., Li, J. Z., & Liu, H. 2014, *ApJ*, 797, 40
- Zavagno, A., Anderson, L. D., Russeil, D., et al. 2010, *A&A*, 518, L101